Matter

CellPress

Article

Disturbance-Promoted Unconventional and Rapid Fabrication of Self-Healable Noble Metal Gels for (Photo-)Electrocatalysis

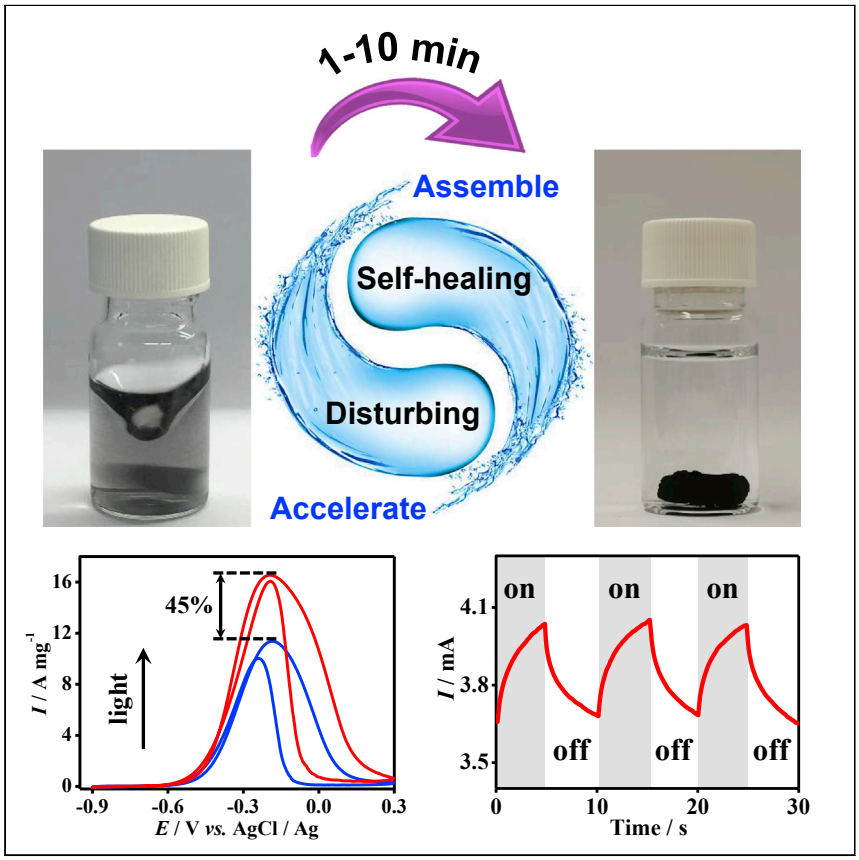

The unusual self-healing behavior of the noble metal gels is revealed, based on which an unconventional disturbance-promoted gelation method is proposed. On this basis, the diffusion limit in the gelation process is overcome, thus producing various monolithic noble metal gels within 1–10 min, which is 2–4 orders of magnitude faster than most previously reported methods. Moreover, the photoelectrocatalytic properties of noble metal aerogels are pioneered, whereby the light considerably promotes the electrocatalytic properties.

Benchmark
First qualification/assessment of material properties and/or performance

Ran Du, Jan-Ole Joswig, Xuelin Fan, René Hübner, Daniel Spittel, Yue Hu, Alexander Eychmüller

dr1581@foxmail.com (R.D.)
alexander.eychmueller@chemie.tu-dresden.de (A.E.)

HIGHLIGHTS

The self-healing behavior of the noble metal gels is revealed

An unconventional disturbance-promoted gelation method is proposed

Various monolithic noble metal gels are created within 1–10 min

The photoelectrocatalytic properties of noble metal aerogels are pioneered

Du et al., Matter 2, 908–920
April 1, 2020
https://doi.org/10.1016/j.matt.2020.01.002

Matter

CellPress

Article

Disturbance-Promoted Unconventional and Rapid Fabrication of Self-Healable Noble Metal Gels for (Photo-)Electrocatalysis

Ran Du,[1,*] Jan-Ole Joswig,[2] Xuelin Fan,[1] René Hübner,[3] Daniel Spittel,[1] Yue Hu,[4] and Alexander Eychmüller[1,5,*]

SUMMARY

As an emerging class of porous materials, noble metal aerogels (NMAs) have drawn tremendous attention and displayed unprecedented potential in diverse fields. However, the development of NMAs is impeded by the fabrication methods because of their time- and cost-consuming procedures, limited generality, and elusive understanding of the formation mechanisms. Here, by revealing the self-healing behavior of noble metal gels and applying it in the gelation process at a disturbing environment, an unconventional and conceptually new strategy, i.e., a disturbance-promoted gelation method, is developed by introducing an external force field. It overcomes the diffusion limitation in the gelation process, thus producing monolithic gels within 1–10 min at room temperature, 2–4 orders of magnitude faster than for most reported methods. Moreover, versatile NMAs are acquired by using this method, and their superior (photo-)electrocatalytic properties are demonstrated for the first time in light of combined catalytic and optic properties.

INTRODUCTION

Aerogels are a class of self-supported, highly porous, three-dimensional (3D) networked materials.[1–3] Combining their structural features and undefined chemical nature, their functions can be versatilely tailored by tuning their composition (e.g., with silica, polymers, nanocarbons, and metals[4–7]), thus unlocking a widespread application potential ranging from thermal insulators, energy storage, and conversion, to environment remediation. Particularly for the recently emerging noble metal aerogels (NMAs), the noble-metal-structured networks afford abundant optically/catalytically active sites as well as 3D electron/mass transfer expressways, thus attracting increasing attention with their unprecedented potential particularly in electrocatalysis, surface-enhanced Raman scattering, and sensing.[8–14]

Despite impressive prospects, the fabrication of NMAs remains challenging, which accounts for their sluggish development in the last decade. The core of the aerogel fabrication lies in the preparation of the wet gel via a sol-gel process. For broad material systems, the formation of a monolithic gel usually requires undisturbed conditions to allow the gradual formation of continuous 3D networks, while this undisturbed condition exerts a large diffusion barrier, thus considerably slowing down the gelation process. Especially for the noble metal systems, very long gelation time (up to several weeks) is frequently observed, not to mention other issues, such as the costly concentration process (i.e., ultracentrifugation), the limited generality, and the elusive understanding of the corresponding formation mechanisms.[9,11,15–21] These problems not only impede a facile

Progress and Potential

Gels are functional materials almost exclusively prepared in an undisturbed environment, so as to afford an intact three-dimensional network. However, the corresponding retarded mass transfer inevitably leads to sluggish reaction kinetics. Particularly for noble metal systems, the gelation can take a few weeks from a dilute precursor solution at room temperature, discouraging the material synthesis and subsequent applications. Here, revealing the self-healing nature of noble metal gels, an unconventional disturbance-promoted gelation method is developed to overcome the diffusion limit in the gelation process, which produces monolithic gels within 1–10 min and is capable of acquiring gels with various compositions and special structures (e.g., core-shell structure). Moreover, photoelectrocatalysis over noble metal aerogels is pioneered by utilizing their combined catalytic and optical properties. These findings may revolutionize both the fundamental and application-oriented research for broad gel systems.

synthesis and the available material systems but also discourage mechanism-oriented manipulation and tailoring of NMAs, thus hindering both the fundamental research and the practical applications.

In the past few years, the aforementioned issues have been partially resolved by continuous methodology development. For example, a $NaBH_4$-mediated one-step reduction method was developed to obtain Pd and/or Pt gels directly from dilute metal salt solutions (metal salt concentration c_M = 0.2 mM) in 3–17 days, avoiding the concentration step.[16] Lin's group further cut down the gelation time to 6 h by applying an elevated temperature (333 K).[22] Based on Ca^{2+}-induced electrostatic crosslinking, Wen et al.[18] fabricated Pd gels in 5 min, but at the expense of using highly concentrated nanoparticle (NP) precursor solutions (c_M = 17 mM) prepared by the costly ultracentrifugation technique. Afterward, the same group found that, via unknown mechanisms, dopamine can efficiently trigger the formation of gold gels within 6–72 h from dilute solutions (c_M = 0.2 mM) at room temperature.[23] Very recently, taking advantage of specific ion effects, we introduced a platform by which the physical picture of the overall gelation process was unveiled, and various tunable noble metal gels were obtained from a wide concentration window (c_M = 0.02–2.0 mM) in a few hours to a few days.[24]

Although considerable progress has been made and various high-performance NMAs have been developed, two serious challenges remain. First, a sufficiently fast gelation process (e.g., <10 min) at a low-to-medium metal concentration (e.g., c_M < 1.0 mM) has never been realized at room temperature, thus posing a large barrier blocking facile material synthesis. Second, the application scope of NMAs is largely restricted to electrocatalysis by utilizing their catalytic activities while overlooking their unique optic features. Recently, we noticed long-term reactivity of gold aggregates/gels, that is, they assembled together during and even after the gelation process.[24] In this regard, here we further disclose the underlying mechanism behind this phenomenon—the self-healing property—and subtly apply it to the gelation process, with which an unconventional and conceptually new method, i.e., the disturbance-promoted gelation strategy, is developed by introducing an external force field during the preparation process. By applying a disturbing environment (e.g., stirring) to break the diffusion limit during the gelation process and then assembling the gel pieces together mediated by their self-healing properties, a monolithic gel was obtained within 1–10 min from a wide concentration window (c_M = 0.02–5.0 mM), which is 2–4 orders of magnitude faster than most reported methods. The presented method is quite universal, fitting diverse initiating approaches, chemical compositions (e.g., Au, Ag, Pd, Rh, Au-Ir, Au-Pd-Pt), and microstructures (e.g., random-distributed and core-shell structures). Moreover, taking advantage of the combined optic and catalytic activities of noble metals, the photoelectrocatalytic properties of NMAs are demonstrated for the first time by using ethanol oxidation reaction (EOR) as a model reaction, displaying an activity increase of up to 45.5% by illumination and realizing a current density of up to 7.3-fold higher than that of commercial Pd/C. Therefore, the present work may open up new space for fundamental and application studies with NMAs as well as other gel systems.

RESULTS AND DISCUSSION

Stirring-Promoted Rapid Sol-Gel Process

Conventionally the sol-gel process proceeds under undisturbed conditions for all material systems to ensure a static environment, allowing the formation of intact and self-supported 3D networks. However, the static environment can strongly

[1]Physical Chemistry, Technische Universität Dresden, Bergstrasse 66b, 01069 Dresden, Germany

[2]Theoretische Chemie, Fakultät für Chemie und Lebensmittelchemie, Technische Universität Dresden, 01062 Dresden, Germany

[3]Helmholtz-Zentrum Dresden-Rossendorf, Institute of Ion Beam Physics and Materials Research, Bautzner Landstrasse 400, 01328 Dresden, Germany

[4]College of Chemistry and Materials Engineering, Wenzhou University, Wenzhou 325000, China

[5]Lead Contact

*Correspondence: dr1581@foxmail.com (R.D.), alexander.eychmueller@chemie.tu-dresden.de (A.E.)

https://doi.org/10.1016/j.matt.2020.01.002

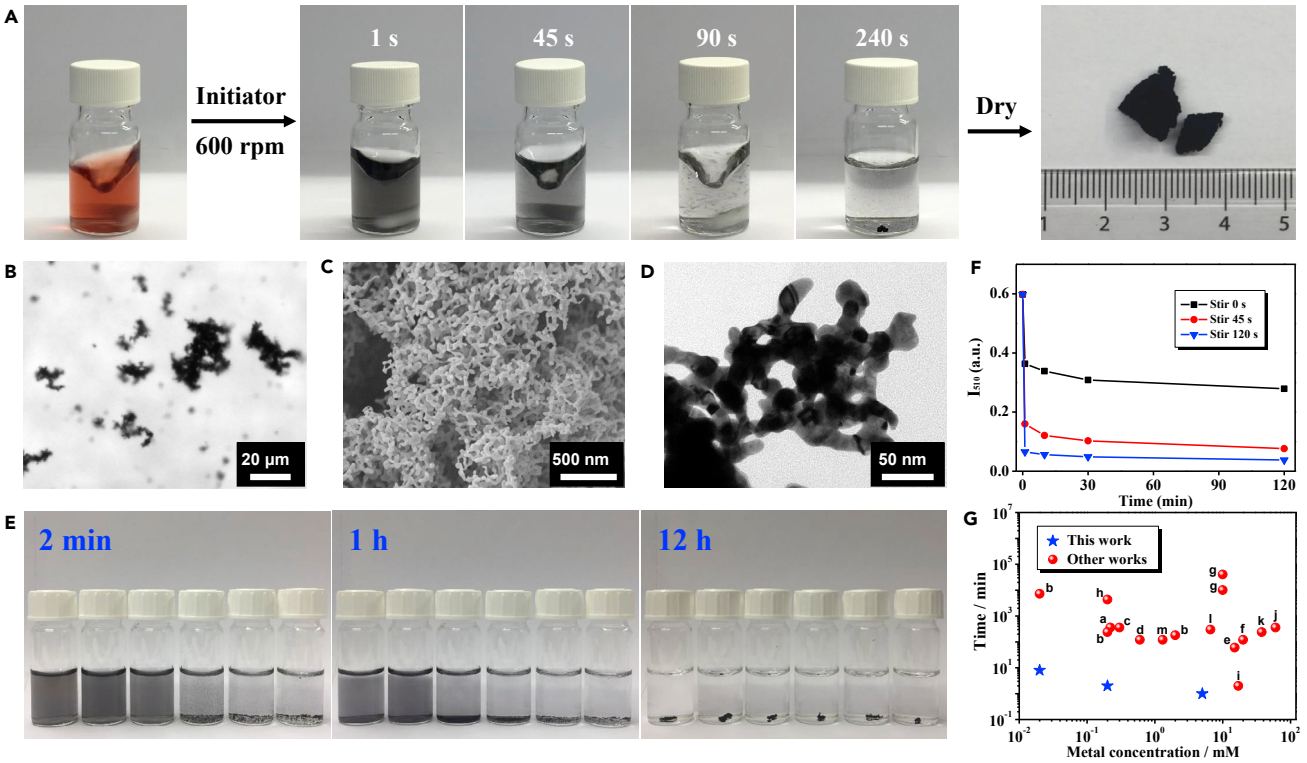

Figure 1. Demonstration and Characterization of the Stirring-Promoted Rapid Fabrication of Gold Gels

(A) Photographs of the stirring-directed gelation process of a gold NP solution (0.2 mM, 10 mL, left) induced by NH_4F and the corresponding aerogel (right). For a better demonstration, the aerogel was created from ~800-mL solutions.

(B) Optical microscopy image of the as-formed gold aggregates after stirring for 45 s.

(C and D) SEM image (C) and TEM image (D) of the obtained gold aerogel.

(E) The gelation process of gold NP solutions under stirring at 600 rpm for 0, 10, 30, 60, 90, and 120 s.

(F) Time-lapse UV-vis absorption intensities obtained at 510 nm for the gelation system under stirring at 600 rpm for 0, 45, and 120 s.

(G) Summary of the gelation time of noble metal gels reported in the literature and in this work versus the initial metal salt concentrations (c_M). References denoted by red dots: a, Wen et al.;[23] b, Du et al.;[24] c, Zhu et al.;[22] d, Shi et al.;[30] e, Naskar et al.;[20] f, Tang et al.;[8] g, Bigall et al.;[10] h, Liu et al.;[15] i, Wen et al.;[18] j, Cai et al.;[19] k, Gao et al.;[17] l,Yazdan-Abad et al.;[31] m, Shi et al.[21]

retard the mass transfer, thus placing a large diffusion barrier that slows down the gelation process. Only for a few organic gel systems, the sol-gel transition was induced by disturbances (i.e., sonication) due to the morphology change of the aggregates during this process.[25,26] Here, we show that in the inorganic world, e.g., for noble metal systems, various disturbing conditions can be applied to overcome the diffusion-limited gelation process and to yield self-supported gels by taking advantage of their self-healing properties. The self-healing behavior, in fact, is also rarely observed in sole inorganic systems without deliberately introducing reversible covalent[27] or non-covalent bonds.[28,29]

In the present work, as an example, the disturbance-promoted gelation process is demonstrated for a dilute gold NP system (gold salt concentration c_M = 0.2 mM). Stirring, which can produce a shearing field, was introduced to create a disturbing environment because of its facileness and good controllability. As illustrated in Figure 1A and Videos S1 and S2, upon initiation of the destabilization by a salting-out method (NH_4F was used as the initiator), the gold NP solution instantly transferred from red to black, suggesting the formation of nanostructured gold aggregates. With further stirring, visible aggregates appeared after ca. 45 s, the reaction was almost completed at 90 s, and a monolithic gel evolved within 4 min assisted by

manually assembling the as-formed self-healable "gel pieces." Following purification and freeze-drying, self-supported aerogels were obtained with a yield of 86.9%. The formation of large gold aggregates after 45 s is also confirmed by optical microscopy imaging, as shown in Figure 1B. A close-up inspection of the resulting gel by scanning electron microscopy (SEM) and transmission electron microscopy (TEM) revealed the highly porous structure, which is similar to those from gels fabricated in an undisturbed environment (Figures 1C, 1D, S1, and S2).

The disturbance can considerably enhance the mass transfer, thus reducing the diffusion barrier and greatly promoting the gelation process. To clarify the effect of disturbance, we investigated the input "disturbing power," expressed by the stirring time and stirring speed. As seen from Figures 1E and S3, both the elongation of the stirring time and increase of the stirring speed considerably promoted the destabilization process. A similar trend was also observed by using other initiating methods (Figure S4). The acceleration behavior was further semi-quantitatively characterized by UV-visible (UV-vis) absorption spectroscopy (Figures 1F and S5), whereby 39%, 73%, and 89% absorption intensity decay (recorded at a wavelength of 510 nm) were observed after successive NH_4F initiation, stirring (for 0, 45, and 120 s, respectively), and grounding for 1 min. With prolonged grounding time until 120 min, the absorption intensity decay of the undisturbed system was only 53%, much less than that of the stirred systems (87% and 94% for 45-s and 120-s stirring, respectively). The above results unambiguously point out that the destabilization process of a gold NP solution is strongly promoted by applying a disturbing environment, where the gelation speed is positively correlated with the degree of disturbance. More impressively, the disturbance-promoted gelation process adapts to a broad concentration window c_M, spanning from 0.02 to 5.0 mM and keeping the gelation time within 1–10 min. As summarized in Figure 1G and Table S1, compared with most previously reported strategies, the presented method remarkably accelerates the gelation speed of the gold system by 2–4 orders of magnitude, allowing the ultrafast and facile acquirement of noble metal gels without elevated temperatures or a concentrating step. Notably, besides introducing a shearing field by stirring, various other disturbance methods, such as manually shaking and bubbling, can be applied to prepare monolithic gels and display similar results (Figures 2A and 2B).

Mechanisms of Disturbance-Promoted Gelation Mediated by Self-Healing Properties

It is not surprising that a disturbing environment can accelerate the reaction by prompting collisions between the reactants, while it is fascinating to see that the fragmented products—visible large aggregates (called gel pieces)—can assemble into a monolithic gel after terminating the disturbance. Previously we found that the gold species (intermediate aggregates or as-formed gels) are highly active throughout the gelation process, thus enabling the final formation of a monolithic gel at the bottom of the vessel due to gravity-driven aggregate sedimentation and assembly.[24] The high-reactivity-enabled assembly of the gold species let us recall the well-known self-healing behavior. Inspired by this, the idea comes naturally that by taking advantage of the high reactivity of the gold species, it is possible to accelerate the reaction in a disturbing environment and subsequently reassemble the resulting products into a monolithic gel under undisturbed conditions, thus harnessing the contradiction between the reaction kinetics and the self-supported materials.

In the first place, the self-healing behavior of noble metal hydrogels is studied. The self-healing properties are almost exclusively found in organic or organic-inorganic

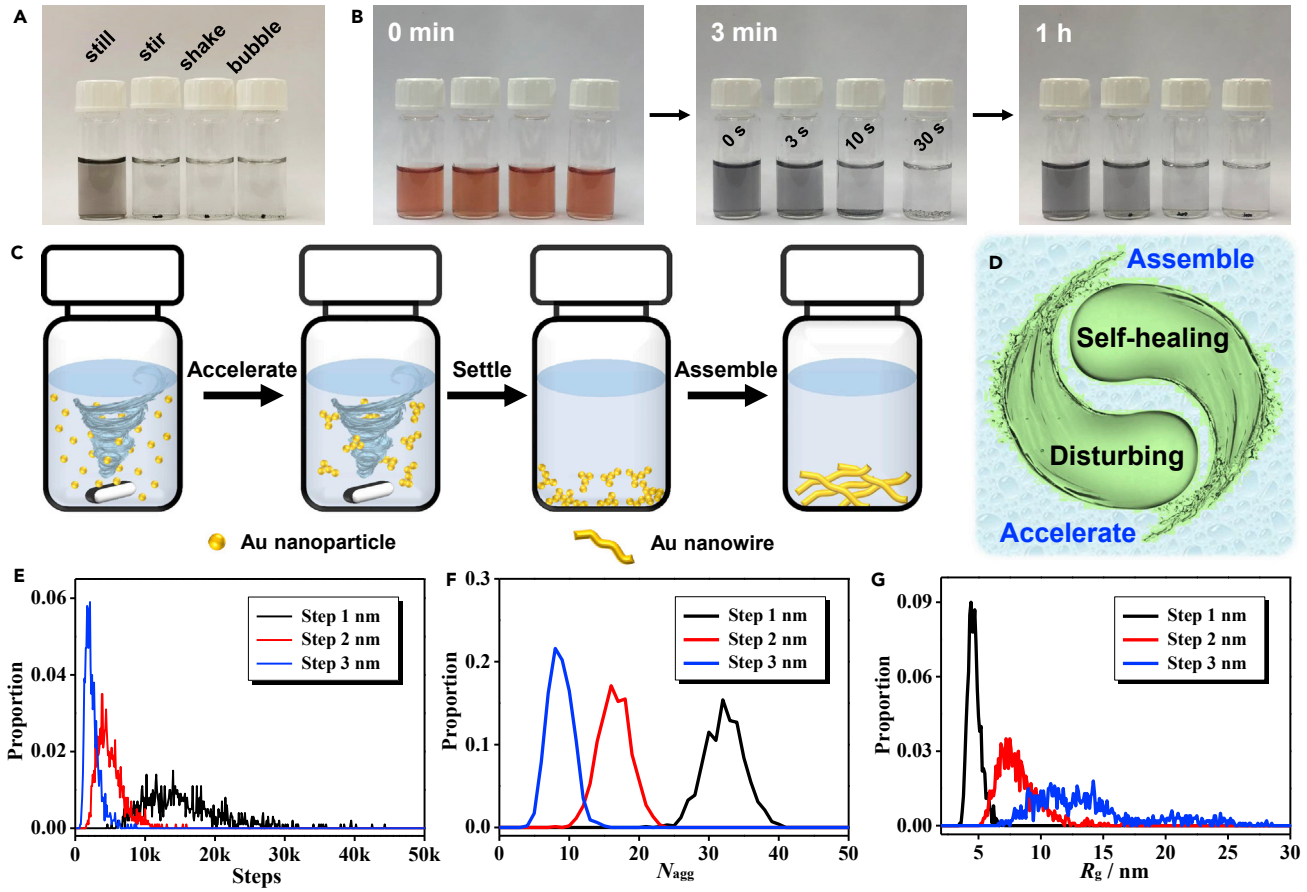

Figure 2. The Mechanisms for the Disturbance-Promoted Gelation

(A) Gold NP solutions destabilized by NH_4F in different environments (undisturbed, stirring for 2 min, shaking for 20 s, and bubbling for 2 min with N_2). The photo was taken 2 min after the corresponding treatment.

(B) Time-lapse photographs of the disturbing-promoted gelation process of gold NP solutions (triggered by NH_4F) by manually shaking for 0, 3, 10, and 30 s.

(C and D) Proposed model for stirring-promoted gelation (C) and the role of the self-healing properties and the disturbing environment played in this process (D).

(E–G) MC simulation under different disturbing conditions (simulated for different maximum step lengths). Distribution of (E) the required steps to form one single aggregate, (F) the number of aggregates after 5,000 MC steps, and (G) the average radius of gyration (R_g) of the resulting aggregates after 15,000 MC steps.

hybrid systems that involve specially devised reversible crosslinking forces (e.g., hydrogen bonds and dynamic chemical bonds),[27,29] while it is rarely observed in sole inorganic systems without delicately introduced interactions. Here, the NH_4F-induced gelation of trisodium citrate (NaCA)-stabilized gold NPs is taken as an example for the discussion. As seen from Figures S6 and S7, the vigorous mechanical disturbance during the gelation did not affect the final formation of a monolithic gold hydrogel, inferring that the gold aggregates/hydrogels maintain high reactivity, i.e., the self-healing properties, during and after the gelation process. Moreover, the gold hydrogels are capable of healing themselves in either the original gelation solution, deionized water, or ethanol, implying that instead of interacting with "healing agents" (e.g., gold species, ligands, reductants) from the initial gelation environment, the self-healing properties should arise from the reversible interactions between the gold building blocks. However, due to the uncontrollable shape of the gold hydrogel because of its mechanical fragility, the quantification of such self-healing properties by rheology and other techniques remains to be tackled.

Second, combining the intriguing self-healing behavior of the gold hydrogels and the disturbance-induced acceleration during the gelation process, a model depicting the formation of monolithic gels is schemed in Figures 2C and 2D. The addition of initiators induces the aggregation and assembly of gold NPs, the process of which is greatly accelerated by applying a disturbing environment such as vigorous stirring. The disturbance can on the one hand enhance the mass transfer and accelerate the reaction speed, while on the other hand restricting the unlimited growth of the gold aggregates due to mechanical crushing, thus leading to the formation of many small gel pieces in the bulk solution. Afterward, the disturbance is removed and the gel pieces can be manually gathered together to form a monolithic gel due to their self-healing properties. In this way, the synergy of disturbance-induced acceleration and self-healing-mediated assembly affords an ultrafast fabrication of monolithic gels in a few minutes.

To intuitively demonstrate the proposed acceleration effect, we apply random-walk Monte Carlo (MC) simulations (Figures 2E, 2F, and S8). In brief, non-interacting particles are allowed to move randomly in a spherical space, and particles that meet during movement are considered as a single aggregate. The algorithm is terminated when all particles are aggregated into a single aggregate, and statistical analysis is performed over 1,000 simulations per parameter set. The disturbing condition is simulated by using different maximum step lengths (x, representing the maximum value of one step) for the particles, while the gelation time is reflected by the required MC steps for all particles to form one aggregate. As seen from Figure 2E, increasing the maximum step length (x = 1, 2, 3 nm) results in a smaller number of MC steps to form a single aggregate as evidenced from the respective probability distribution curves, which reflect a shorter gelation time with a more intensive disturbance. For a fixed step number, i.e., a specific period of reaction time, the amount of remaining aggregates (N_{agg}) and the average radius of gyration (R_g) are negatively and positively correlated with x, respectively (Figures 2F, 2G, and S8), suggesting that an enhanced disturbance can accelerate the reaction and thus form larger aggregates, which further portrays the disturbance-directed acceleration of the gelation process. In addition, after formation of a single aggregate, it is found that a larger maximum step length x resulted in a smaller R_g, inferring an increase of density for the gel fabricated under disturbance (Figure S9). This is in line with the experimental results showing that the stirring-produced gold aerogel exhibited a density much larger than the one prepared under non-disturbed conditions[24] (309.1 mg cm^{-3} versus 108.7 mg cm^{-3}).

Generality of the Disturbance-Promoted Gelation Method

Introducing a disturbing environment to substantially accelerate the gelation process is a general strategy that is compatible with various initiation approaches and fits diverse systems. As seen from Figures 3A–3C, the stirring-promoted gelation of gold gels works well for a broad concentration range (c_M = 0.02–5 mM), various ligand-stabilized gold NPs (e.g., ligand-free, NaCA, β-alanine, polystyrene sulfonate, polyvinylpyrrolidone [PVP]), and versatile initiators (e.g., NH_4NO_3, NaOH, KNO_3, and $NaBH_4$). In this way, the structure parameters of the resulting gold aerogels can be flexibly tuned (Figure S10 and Table S2). For example, compared with the NH_4F-induced gelation of NaCA-stabilized gold NPs, the aerogel made from $NaBH_4$-destabilized PVP-coordinated gold NPs displayed a reduced ligament size from 19.8 ± 3.7 nm to 10.4 ± 3.1 nm, presumably due to the PVP-directed oriented growth,[32] thus resulting in a high specific surface area (SSA) of 42.6 $m^2\ g^{-1}$, surpassing that of most previously reported porous gold materials (<1 to 30 $m^2\ g^{-1}$)[10,12,24,33–35] and only slightly lower than that of a gold-β-cyclodextrin aerogel (50.1 $m^2\ g^{-1}$, with ~18 wt % β-cyclodextrin[23]).

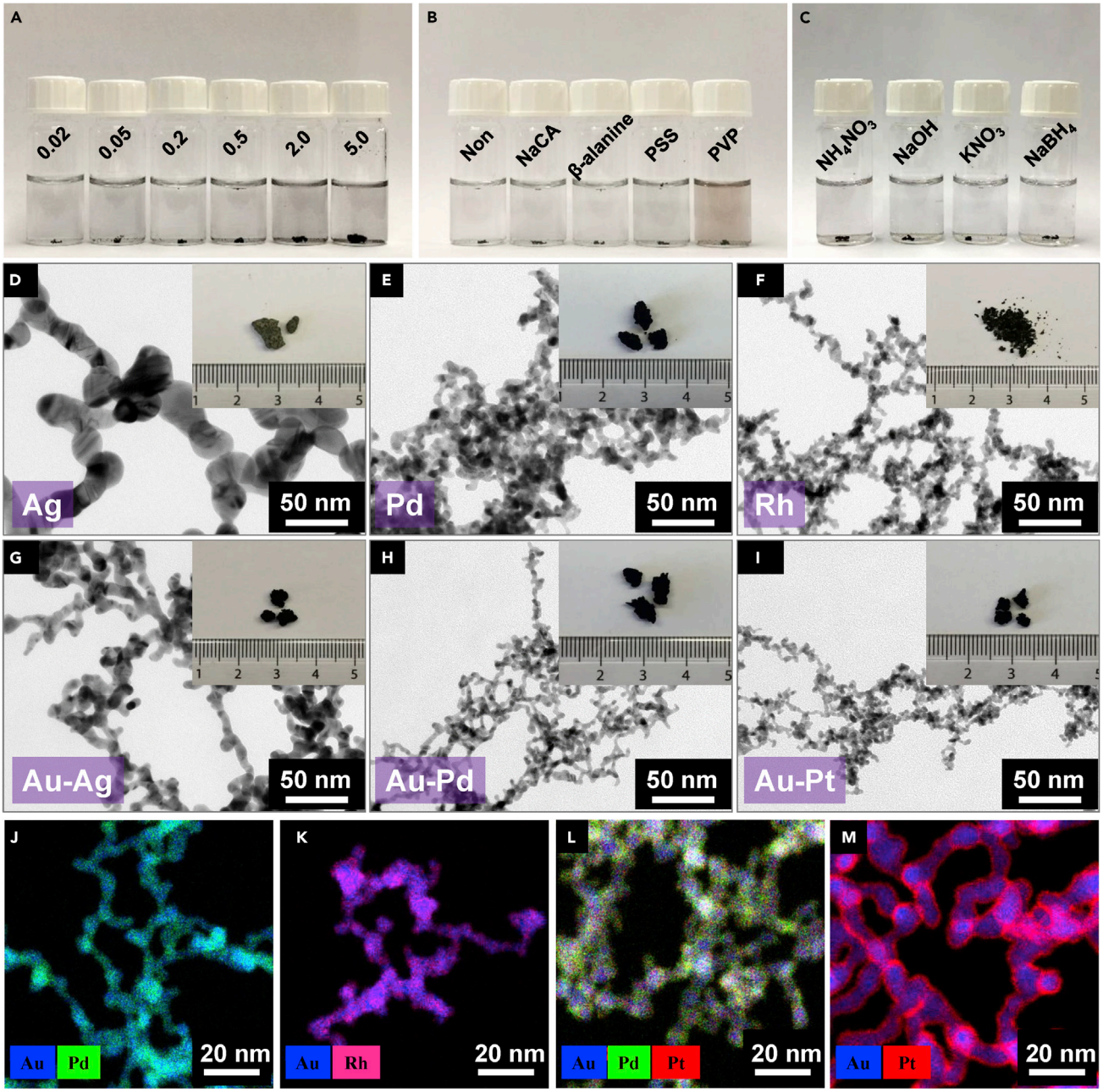

Figure 3. Generality of the Disturbance-Promoted Gelation

(A–C) Stirring-promoted gelation of diverse gold gels. (A) $NaBH_4$-initiated gelation from NaCA-stabilized gold NP solutions with c_M ranging from 0.02 mM to 5.0 mM, (B) $NaBH_4$-initiated gelation from gold NP solutions stabilized by different ligands (c_M = 0.2 mM), and (C) gelation of NaCA-stabilized gold NP solutions triggered by different initiators (c_M = 0.2 mM).

(D–I) NMAs with different compositions. (D) Ag, (E) Pd, (F) Rh, (G) Au-Ag, (H) Au-Pd, and (I) Au-Pt. The inset photograph in (F) shows the residual of the Rh aerogel after spontaneously burning in air.

(J–M) Energy-dispersive X-ray mapping of multimetallic aerogels made of (J) Au-Pd, (K) Au-Rh, (L) Au-Pd-Pt, and (M) core-shell Au-Pt. (J), (K), and (L) were prepared by a two-step method, while (M) was prepared by the dynamic shelling approach.

Moreover, the disturbance-promoted acceleration can be extended to NMAs with versatile compositions such as Ag, Pd, Rh, Au-Ag, Au-Pd, Au-Pt, Au-Rh, and Au-Pd-Pt, with a reasonable yield of >75% for all mentioned systems, which is acceptable compared with the yield obtained under undisturbed conditions (typically

>90%). The yield might be further increased by a more careful operation or a prolonged time for the gel-assembling process. The resulting aerogels were characterized by electron microscopy, X-ray diffraction, and X-ray photoelectron spectroscopy (XPS) (Figures 3D–3I and S11–S16; Table S2). Similar to previous observations,[24] the Ag aerogel manifested a large ligament size (18.1 ± 3.0 nm), considerably thicker than that of the single-metallic Pd (5.8 ± 1.2 nm) and Rh (4.1 ± 0.5 nm) aerogels, as well as the multimetallic Au-Ag (7.1 ± 1.0 nm), Au-Pd (3.9 ± 0.6 nm), Au-Pt (3.7 ± 0.7 nm), Au-Rh (4.6 ± 1.2 nm), Au-Ir (7.2 ± 1.8 nm), and Au-Pd-Pt (4.3 ± 0.6 nm) aerogels. The various ligament sizes along with the chemical compositions further influenced the SSAs and the pore volumes of NMAs, which are located in the range of 5.6–83.6 $m^2\ g^{-1}$ and 0.1–0.9 $cm^3\ g^{-1}$, respectively (Figures S17–S19 and Table S2). As seen from the pore-size distribution, the presence of predominant mesopores (mostly 3–10 nm) should offer numerous active sites while simultaneously maintaining a fast mass transfer, which is beneficial for applications such as electrocatalysis.

For the multimetallic systems, the spatial element distribution cannot be well predicted by using the two-step method as detailed in Supplemental Information. As seen from Figures 3J–3L, S20, and S21, the Au-Ag and Au-Rh gels displayed core-shell-like structures while the others exhibited random element distributions. The spontaneous formation of the core-shell structure might be attributed to the segregation of low-surface-energy metals on the high-surface-energy ones.[36] To increase the utilization efficiency of the active component, the Au-Pt aerogel with a pronounced core-shell structure was devised by combining our previously reported dynamic shelling approach (DSA)[24] with the currently developed stirring-promoted gelation strategy (Figures 3M and S21), by simply altering the feeding order of the reactants. The successful application of the DSA offers an extremely facile and rapid fabrication strategy toward monolithic noble metal gels with sophisticated microstructures, which is much easier and extremely time-saving compared with previously reported approaches, such as pre-NP-engineering or sequential gel fabrication-underpotential decomposition-galvanic replacement methods.[14,19]

Electrocatalysis and Photoelectrocatalysis by NMAs

Featuring stable 3D networks, continuous electron/mass transfer highways, controlled spatial element distribution, and abundant active catalytic sites, NMAs have been widely explored in various electrocatalytic processes, such as alcohol oxidation, oxygen reduction reaction, and oxygen evolution reaction.[14,21,22,30,37,38] On the other hand, noble metal nanostructures feature unique optic properties, which allows coupling between the collective surface electron oscillations and the incident electromagnetic field,[39] thus yielding a dramatically enhanced localized electric field for surface-enhanced Raman scattering.[8] However, the plasmonic-assisted photoelectrocatalysis properties, which entered the vision of the scientific community in recent years, have not been explored for NMAs so far.

Here, the ethanol oxidation is adopted as a model reaction, whereby the electrocatalytic performance under dark conditions is investigated first. As shown in Figure 4A, the peak appearing in the forward scan and the backward scan mark the oxidation of the ethanol and the oxidation of the intermediate generated during the forward scan, respectively, where the forward current density (I_f) and the ratio of the forward/backward current density (I_f/I_b) are the two important parameters accounting for the EOR performance.[30] The difference of the peak positions obtained from various catalysts can be attributed to the different reaction pathways presented in

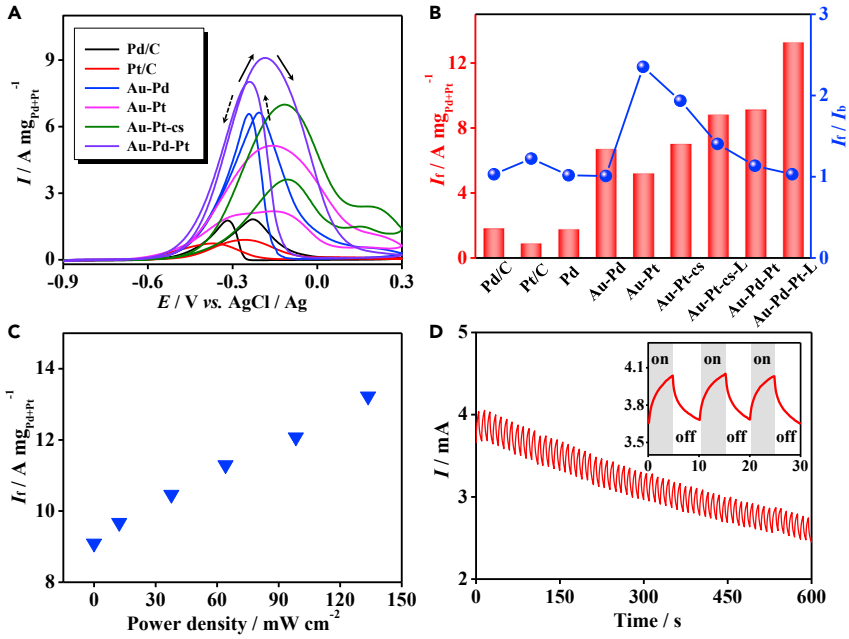

Figure 4. Application of NMAs in Electrocatalysis and Photoelectrocatalysis

(A) Electrocatalytic performance of the EOR with commercial and various aerogel catalysts.

(B) Summarized I_f and I_f/I_b of various catalysts. Au-Pt-cs denotes the core-shell-structured Au-Pt aerogel, and the suffix "L" denotes that the test was conducted under white-light illumination at 133.6 mW cm^{-2}.

(C) Dependence of I_f of the Au-Pd-Pt aerogel on the input light power density.

(D) Light response behavior on an Au-Pd-Pt aerogel electrode in the course of a chronoamperometry test. All tests were performed in nitrogen-saturated 1.0 M KOH + 1.0 M ethanol aqueous solution.

the respective systems, while the details remain to be deeply investigated. As summarized in Figure 4B, except for the Pd aerogel, all other Pd- and Pt-based multimetallic aerogels displayed considerably higher activity than that of the commercial Pd/C or Pt/C catalysts (1.8 A mg_{Pd}^{-1} and 0.9 A mg_{Pt}^{-1}). In particular, the delicately designed Au-Pt core-shell aerogel exhibited an I_f of 7.3 A mg_{Pt}^{-1}, and the Au-Pd-Pt trimetallic aerogel showed an even higher I_f of 9.1 A mg_{Pd+Pt}^{-1}, indicating the advantages of the delicately devised core-shell structure and/or the synergistic effect from multiple elements. On the other hand, a substantially high I_f/I_b is observed for the Au-Pt (2.35) and the Au-Pt core-shell aerogel (1.93), roughly double that of the other commercial and aerogel catalysts (1.00–1.22), thus indicating high efficiency in the forward oxidation step for the gold-platinum bimetallic systems. Although a rapid current decay was observed for all systems, NMA-based electrocatalysts manifested a much better stability compared with that of the commercial ones (current retention of 19.6%–32.9% versus 1.2%–5.7% for a 2,000-s operation), which can be attributed to the stable 3D networks feature of NMAs (Figure S22).

Taking advantage of the unique optical properties of the noble metal nanostructures (especially Au and Ag),[39,40] the photoelectrocatalytic properties of EOR have been primarily investigated. With a commercial white-light LED source, the electrocatalytic EOR on commercial- and aerogel-based noble metal catalysts has been explored under dark and light conditions (133.6 mW cm^{-2}), as shown in Figures 4B and S23. In virtue of the light-assisted performance enhancement, 12.4% and 15.9% increase in I_f was observed for Pt/C and Pd/C, respectively, while

improvements of >20% were observed for the aerogel systems. However, the I_f/I_b ratio is slightly reduced for all systems, except for Pt/C and the Pd aerogel. Impressively, the Au-Pd-Pt aerogel manifested a 45.5% current density enhancement upon illumination, reaching a remarkably high I_f of 13.2 A mg_{Pd+Pt}^{-1}, which is 7.3-fold higher than that of commercial Pd/C and surpasses most NMAs such as Pd, Pd-Ni, and Au-Pd-Pt aerogels (2.3–6.1 times higher than Pd/C),[15,19,24,31] and being only lower than the Pd-ensembles-anchored Au-Cu aerogel (11.6 times higher than Pd black).[30] The Au-Pt core-shell aerogel also displayed a substantially high I_f of 8.8 A mg_{Pd+Pt}^{-1}, and concurrently maintained a fairly high I_f/I_b of 1.4. The high performance of these NMAs can be attributed to the synergy of high catalytic activity of Pd/Pt, and high electrical conductivity of Au, as well as strong optic absorption of all nanostructured metals. Further experiments on the Au-Pd-Pt aerogel indicate that the I_f is positively correlated with the light power density, and the presented light-promoted catalysis might be applied for photosensing with a sensitivity of >40.2 μA mW^{-1} (Figures 4C and 4D). In contrast, on a bare glassy carbon electrode, no visible oxidation peak was observed (Figure S23), either in darkness or under light, indicating the indispensable role of the noble metal nanostructures.

The photoelectrocatalytic process has long been focused on semiconductor-based systems, while studies on noble metal nanostructures, which are usually used as co-catalysts in conjunction with semiconductors to enhance light harvesting or promote charge transfer, only appeared recently.[38,39,41,42] The enhancement mechanism by noble metal nanostructures can be attributed to localized surface plasmon resonances (LSPR), light absorption by nanostructures-induced trapping, and the intraband transition.[42] As opposed to most other materials, the surface electrons of noble metal nanostructures can be oscillated upon irradiation with incident light of appropriate wavelength (i.e., LSPR), strongly enhancing the light field and generating hot carriers (electron-hole pair), or by electron-phonon coupling (i.e. heat dissipation) upon de-excitation.[39] Hence, three mechanisms including (1) enhanced photon density, (2) hot-carrier transfer, and (3) plasmonic thermal effect may account for the increase in plasmon-assisted performance.[40] Because of the application of a white-light source (wavelength 350–800 nm) in this study (covering a wide wavelength range), none of those mechanisms can be ruled out. On the other hand, for the non-plasmon-absorption region, light trapping by metal nanostructures may incur a heat effect via the multiple absorption and scattering of the incident light,[24] also contributing to the catalytic enhancement. The decoupling and careful characterization of the contributions in the photoelectrocatalytic process, the further enhancement of the light-assisted catalytic performance possibly by engineering the plasmonic absorption behavior of the aerogels, and the expansion of available catalytic reactions will be future directions for NMA-based photoelectrocatalysis research.

Conclusion

In the field of NMAs, many synthesis-related challenges, including cost- and time-consuming procedures and the debated gel-formation mechanisms, have largely discouraged the material design and the application diversity of NMAs. In this work, by disclosing the self-healing behavior of the noble metal hydrogels and subtly applying it in the gelation process, an unconventional and conceptually new method, i.e., disturbance-promoted gelation, is developed by introducing an external force field. This approach is capable of breaking the diffusion barrier in the gelation process and thus acquiring monolithic gels within 1–10 min without elevated temperatures or preconcentrating step, which is 2–4 orders of magnitude faster than for most methods reported. To understand the self-healing-property-mediated disturbance-promoted

process, MC simulations have been performed, whereby the statistics of the aggregation behaviors unambiguously point out the acceleration mechanisms. Notably, the developed strategy is compatible with various initiation methods, thus affording a library of monolithic gels with widespread ligament sizes (3.7–19.8 nm), compositions (Au, Ag, Pd, Rh, and versatile multimetallic alloys), and spatial element distributions (e.g., random-distributed and core-shell structures). Finally, taking advantage of the unique optical properties of nanostructured noble metals, photoelectrocatalytic ethanol oxidation has been studied, whereby the Au-Pd-Pt and the Au-Pt core-shell aerogels, under illumination at 133.6 mW cm^{-2}, exhibited I_f of 7.3- and 4.9-fold, and I_f/I_b ratios 1.05- and 1.40-fold higher than those of commercial Pd/C. The present work not only provides a counterintuitive yet very efficient gelation method that may be expanded to various gel systems, but also pioneers the exploration of photoelectrocatalysis on NMAs, thus opening up new space for both fundamental and application-oriented studies of noble metal gels and other systems.

EXPERIMENTAL PROCEDURES

Synthesis Methodologies

Noble metal hydrogels were synthesized by either a one-step method or a two-step method at ambient temperature (~293 K), starting from a metal salt solution and a metal nanoparticle (NP) solution, respectively. As an example for the preparation of gold aerogels via a two-step method, an aqueous solution of NH_4F (10.0 M, 50 μL) was added to the as-prepared trisodium citrate-stabilized gold NP solution (4.95 mL, c_M = 0.2 mM). After continuously stirring for ca. 90 s, the resulting gel pieces were manually assembled together to form a monolithic hydrogel. The as-prepared hydrogel was washed by a large amount of water four to five times with a total duration of 2–3 days to remove possible residues, followed by solvent exchange with *tert*-butanol. Afterward, the wet gel was flash-frozen by liquid nitrogen and subjected to vacuum drying for 12–24 h. The yield of NMAs was calculated based on the mass of the final aerogels with respect to the mass of the corresponding precursor metal salts.

Electrocatalysis and Photoelectrocatalysis

All electrochemical tests were performed with a three-electrode system, with a glassy carbon electrode (3 mm in diameter), an Ag/AgCl (saturated KCl aqueous solution) electrode, and a platinum foil as the working electrode, reference electrode, and counter electrode, respectively. For the electro-oxidation of ethanol, the test was performed under N_2 atmosphere in 1.0 M KOH aqueous solution containing 1.0 M ethanol. CV curves were recorded between −0.9 and 0.3 V (versus AgCl/Ag) with a scanning rate of 50 mV s^{-1}, and the stability test was conducted at a potential of −0.23 V (versus AgCl/Ag). For photoelectrocatalysis, a white LED source was placed perpendicular to the working electrode, affording an adjustable light power density between 0 and 133.6 mW cm^{-2}.

DATA AND CODE AVAILABILITY

All data needed to evaluate the conclusions in the paper are present in the paper and/or Supplemental Information. Additional data related to this paper can be requested from the authors.

SUPPLEMENTAL INFORMATION

Supplemental Information can be found online at https://doi.org/10.1016/j.matt.2020.01.002.

ACKNOWLEDGMENTS

R.D. acknowledges the support from the Alexander von Humboldt Foundation. We thank Dr. Julio Bastos Arrieta for assisting in optical imaging, Dr. Minghao Yu for assisting with the Fourier transform infrared tests, and Shishu Zhang for assisting in XPS measurements. Furthermore, the use of the HZDR Ion Beam Center TEM facilities is acknowledged. The computations were performed on an HPC system at the Center for Information Services and High Performance Computing (ZIH) at TU Dresden within the project QDSIM. This work was supported by the research funding of the Humboldt fellowship, the ERC AdG AEROCAT, the German Federal Ministry of Education of Research (BMBF, 03SF0451), the China Scholarship Council, the National Natural Science Foundation of China (51972237), and the Natural Science Foundation of Zhejiang Province (LY19E020008).

AUTHOR CONTRIBUTIONS

R.D. conceived the experiments and performed the materials synthesis. J.-O.J. carried out the computational part. Y.H. partially performed SEM, TEM, and XPS analysis. X.F., R.D., and D.S. performed EOR electrocatalysis and photoelectrocatalysis. R.H. performed the scanning TEM energy-dispersive X-ray spectroscopy analysis. R.D. performed all other experimental characterizations or measurements as well as the data analysis. R.D. drafted the manuscript, R.H., J.-O.J., and A.E. revised the manuscript, and all authors commented on the manuscript.

DECLARATION OF INTERESTS

The authors declare no competing interests.

Received: October 9, 2019
Revised: November 18, 2019
Accepted: January 2, 2020
Published: January 29, 2020

REFERENCES

1. Gesser, H., and Goswami, P. (1989). Aerogels and related porous materials. Chem. Rev. *89*, 765–788.
2. Hüsing, N., and Schubert, U. (1998). Aerogels—airy materials: chemistry, structure, and properties. Angew. Chem. Int. Ed. *37*, 22–45.
3. Ziegler, C., Wolf, A., Liu, W., Herrmann, A.-K., Gaponik, N., and Eychmüller, A. (2017). Modern inorganic aerogels. Angew. Chem. Int. Ed. *56*, 13200–13221.
4. Kistler, S.S. (1931). Coherent expanded aerogels and jellies. Nature *127*, 741.
5. Du, R., Zhang, N., Xu, H., Mao, N., Duan, W., Wang, J., Zhao, Q., Liu, Z., and Zhang, J. (2014). CMP aerogels: ultrahigh-surface-area carbon-based monolithic materials with superb sorption performance. Adv. Mater. *26*, 8053–8058.
6. Cai, B., Sayevich, V., Gaponik, N., and Eychmüller, A. (2018). Emerging hierarchical aerogels: self-assembly of metal and semiconductor nanocrystals. Adv. Mater. *30*, 1707518.
7. Du, R., Zhao, Q., Zhang, N., and Zhang, J. (2015). Macroscopic carbon nanotube-based 3D monoliths. Small *11*, 3263–3289.
8. Tang, S., Vongehr, S., Wang, Y., Cui, J., Wang, X., and Meng, X. (2014). Versatile synthesis of high surface area multi-metallic nanosponges allowing control over nanostructure and alloying for catalysis and SERS detection. J. Mater. Chem. A *2*, 3648–3660.
9. Du, R., Fan, X., Jin, X., Hübner, R., Hu, Y., and Eychmüller, A. (2019). Emerging noble metal aerogels: state of the art and a look forward. Matter *1*, 39–56.
10. Bigall, N.C., Herrmann, A.K., Vogel, M., Rose, M., Simon, P., Carrillo-Cabrera, W., Dorfs, D., Kaskel, S., Gaponik, N., and Eychmüller, A. (2009). Hydrogels and aerogels from noble metal nanoparticles. Angew. Chem. Int. Ed. *48*, 9731–9734.
11. Du, R., Jin, X., Hübner, R., Fan, X., Hu, Y., and Eychmüller, A. (2019). Engineering self-supported noble metal foams toward electrocatalysis and beyond. Adv. Energy Mater. https://doi.org/10.1002/aenm.201901945.
12. Nahar, L., Farghaly, A.A., Esteves, R.J.A., and Arachchige, I.U. (2017). Shape controlled synthesis of Au/Ag/Pd nanoalloys and their oxidation-induced self-assembly into electrocatalytically active aerogel monoliths. Chem. Mater. *29*, 7704–7715.
13. Tappan, B.C., Steiner, S.A., and Luther, E.P. (2010). Nanoporous metal foams. Angew. Chem. Int. Ed. *49*, 4544–4565.
14. Cai, B., Hübner, R., Sasaki, K., Zhang, Y., Su, D., Ziegler, C., Vukmirovic, M.B., Rellinghaus, B., Adzic, R.R., and Eychmüller, A. (2018). Core-shell structuring of pure metallic aerogels towards highly efficient platinum utilization for the oxygen reduction reaction. Angew. Chem. Int. Ed. *57*, 2963–2966.
15. Liu, W., Herrmann, A.K., Geiger, D., Borchardt, L., Simon, F., Kaskel, S., Gaponik, N., and Eychmüller, A. (2012). High-performance electrocatalysis on palladium aerogels. Angew. Chem. Int. Ed. *51*, 5743–5747.
16. Liu, W., Rodriguez, P., Borchardt, L., Foelske, A., Yuan, J., Herrmann, A.K., Geiger, D., Zheng, Z., Kaskel, S., and Gaponik, N. (2013). Bimetallic aerogels: high-performance electrocatalysts for the oxygen reduction reaction. Angew. Chem. Int. Ed. *52*, 9849–9852.
17. Gao, X., Esteves, R.J., Luong, T.T.H., Jaini, R., and Arachchige, I.U. (2014). Oxidation-induced self-assembly of Ag nanoshells into transparent

and opaque Ag hydrogels and aerogels. J. Am. Chem. Soc. *136*, 7993–8002.

18. Wen, D., Herrmann, A.-K., Borchardt, L., Simon, F., Liu, W., Kaskel, S., and Eychmüller, A. (2014). Controlling the growth of palladium aerogels with high-performance toward bioelectrocatalytic oxidation of glucose. J. Am. Chem. Soc. *136*, 2727–2730.

19. Cai, B., Wen, D., Liu, W., Herrmann, A.K., Benad, A., and Eychmüller, A. (2015). Function-led design of aerogels: self-assembly of alloyed PdNi hollow nanospheres for efficient electrocatalysis. Angew. Chem. Int. Ed. *54*, 13101–13105.

20. Naskar, S., Freytag, A., Deutsch, J., Wendt, N., Behrens, P., Köckritz, A., and Bigall, N.C. (2017). Porous aerogels from shape-controlled metal nanoparticles directly from nonpolar colloidal solution. Chem. Mater. *29*, 9208–9217.

21. Shi, Q., Zhu, C., Zhong, H., Su, D., Li, N., Engelhard, M.H., Xia, H., Zhang, Q., Feng, S., Beckman, S.P., et al. (2018). Nanovoid incorporated Ir_xCu metallic aerogels for oxygen evolution reaction catalysis. ACS Energy Lett. *3*, 2038–2044.

22. Zhu, C., Shi, Q., Fu, S., Song, J., Xia, H., Du, D., and Lin, Y. (2016). Efficient synthesis of MCu (M= Pd, Pt, and Au) aerogels with accelerated gelation kinetics and their high electrocatalytic activity. Adv. Mater. *28*, 8779–8783.

23. Wen, D., Liu, W., Haubold, D., Zhu, C., Oschatz, M., Holzschuh, M., Wolf, A., Simon, F., Kaskel, S., and Eychmüller, A. (2016). Gold aerogels: three-dimensional assembly of nanoparticles and their use as electrocatalytic interfaces. ACS Nano *10*, 2559–2567.

24. Du, R., Hu, Y., Hübner, R., Joswig, J.-O., Fan, X., and Eychmüller, A. (2019). Specific ion effects directed noble metal aerogels: versatile manipulation for electrocatalysis and beyond. Sci. Adv. *5*, eaaw4590.

25. Liu, Z.-X., Feng, Y., Yan, Z.-C., He, Y.-M., Liu, C.-Y., and Fan, Q.-H. (2012). Multistimuli responsive dendritic organogels based on azobenzene-containing poly(aryl ether) dendron. Chem. Mater. *24*, 3751–3757.

26. Zhang, S., Yang, S., Lan, J., Tang, Y., Xue, Y., and You, J. (2009). Ultrasound-induced switching of sheetlike coordination polymer microparticles to nanofibers capable of gelating solvents. J. Am. Chem. Soc. *131*, 1689–1691.

27. Zhang, Y., Yang, B., Zhang, X., Xu, L., Tao, L., Li, S., and Wei, Y. (2012). A magnetic self-healing hydrogel. Chem. Commun. *48*, 9305–9307.

28. Wang, Q., Mynar, J.L., Yoshida, M., Lee, E., Lee, M., Okuro, K., Kinbara, K., and Aida, T. (2010). High-water-content mouldable hydrogels by mixing clay and a dendritic molecular binder. Nature *463*, 339–343.

29. Du, R., Wu, J., Chen, L., Huang, H., Zhang, X., and Zhang, J. (2014). Hierarchical hydrogen bonds directed multi-functional carbon nanotube-based supramolecular hydrogels. Small *10*, 1387–1393.

30. Shi, Q., Zhu, C., Tian, M., Su, D., Fu, M., Engelhard, M.H., Chowdhury, I., Feng, S., Du, D., and Lin, Y. (2018). Ultrafine Pd ensembles anchored-Au_2Cu aerogels boost ethanol electrooxidation. Nano Energy *53*, 206–212.

31. Yazdan-Abad, M.Z., Noroozifar, M., Alam, A.R.M., and Saravani, H. (2017). Palladium aerogel as a high-performance electrocatalyst for ethanol electro-oxidation in alkaline media. J. Mater. Chem. A *5*, 10244–10249.

32. Koczkur, K.M., Mourdikoudis, S., Polavarapu, L., and Skrabalak, S.E. (2015). Polyvinylpyrrolidone (PVP) in nanoparticle synthesis. Dalton Trans. *44*, 17883–17905.

33. Burpo, F.J., Nagelli, E.A., Morris, L.A., McClure, J.P., Ryu, M.Y., and Palmer, J.L. (2017). Direct solution-based reduction synthesis of Au, Pd, and Pt aerogels. J. Mater. Res. *32*, 4153–4165.

34. Xu, C., Su, J., Xu, X., Liu, P., Zhao, H., Tian, F., and Ding, Y. (2007). Low temperature CO oxidation over unsupported nanoporous gold. J. Am. Chem. Soc. *129*, 42–43.

35. Freytag, A., Sánchez-Paradinas, S., Naskar, S., Wendt, N., Colombo, M., Pugliese, G., Poppe, J., Demirci, C., Kretschmer, I., Bahnemann, D.W., et al. (2016). Versatile aerogel fabrication by freezing and subsequent freeze-drying of colloidal nanoparticle solutions. Angew. Chem. Int. Ed. *55*, 1200–1203.

36. Feng, J., and Yin, Y. (2019). Self-templating approaches to hollow nanostructures. Adv. Mater. *31*, 1802349.

37. Shi, Q., Zhu, C., Du, D., Bi, C., Xia, H., Feng, S., et al. (2017). Kinetically controlled synthesis of AuPt bi-metallic aerogels and their enhanced electrocatalytic performances. J. Mater. Chem. A *5*, 19626–19631.

38. Wang, H., Wu, Y., Luo, X., Jiao, L., Wei, X., Gu, W., Du, D., Lin, Y., and Zhu, C. (2019). Ternary PtRuCu aerogels for enhanced methanol electrooxidation. Nanoscale *11*, 10575–10580.

39. Linic, S., Aslam, U., Boerigter, C., and Morabito, M. (2015). Photochemical transformations on plasmonic metal nanoparticles. Nat. Mater. *14*, 567–576.

40. Zhang, Z., Zhang, C., Zheng, H., and Xu, H. (2019). Plasmon-driven catalysis on molecules and nanomaterials. Acc. Chem. Res. *52*, 2506–2515.

41. Chang, X., Wang, T., Yang, P., Zhang, G., and Gong, J. (2019). The development of cocatalysts for photoelectrochemical CO_2 reduction. Adv. Mater. *31*, 1804710.

42. Liu, L., Zhang, X., Yang, L., Ren, L., Wang, D., and Ye, J. (2017). Metal nanoparticles induced photocatalysis. Natl. Sci. Rev. *4*, 761–780.

Matter, Volume *2*

Supplemental Information

Disturbance-Promoted Unconventional and Rapid Fabrication of Self-Healable Noble Metal Gels for (Photo-)Electrocatalysis

Ran Du, Jan-Ole Joswig, Xuelin Fan, René Hübner, Daniel Spittel, Yue Hu, and Alexander Eychmüller

Experimental Procedures

Reagents and Materials

Reagents including hydrogen tetrachloroaurate (III) ($HAuCl_4 \cdot 3H_2O$), silver nitrate ($AgNO_3$), potassium tetrachloropalladate (II) (K_2PdCl_4), potassium tetrachloroplatinate (II) (K_2PtCl_4), ammonium hexachlororhodate (III) ($(NH_4)_3RhCl_6$), trisodium citrate dihydrate (NaCA), sodium borohydride ($NaBH_4$), polyvinylpyrrolidone (PVP, M_w = 58000), 20% palladium on carbon, and others were purchased from Sigma-Aldrich or Alfa-Aesar. All reagents are used without further purification.

Fabrication of Noble Metal Hydrogels (NMHs)

Hydrogels were synthesized by either a one-step method or a two-step method at ambient temperature (~293 K), which is started from a metal salt solution or a metal nanoparticle (NP) solution. Multimetallic hydrogels were synthesized via a similar route to that for single-metal hydrogels, except that several metal precursor salts were mixed at an equal molar ratio before further reduction and initiation. In comparison to previous reports, after initiation with specific additives (e.g. NH_4F), a prolonged stirring time (1–5 min) or other disturbing approaches were applied for accelerating the gelation process.

One-step method

The fabrication process of a $NaBH_4$-triggered one-step gelation of gold salt solutions is described as an example. Under stirring (e.g., 600 rpm), an aqueous solution of $HAuCl_4 \cdot 3H_2O$ (32.5 mM, 30.8 μL) was added to water (4.87 mL), followed by the addition of freshly prepared $NaBH_4$ aqueous solution (1.0 M, 100.0 μL). After continuously stirring for *ca.* 90 s, the resulting gel pieces were manually assembled together to form a monolithic gel. For the experiments where ligands were included, an aqueous solution of the corresponding ligand (400.0 mM, 25.0 μL) was added before adding the gold salts. The fabrication process can be scaled up to 800 mL, where the stirring time was set to 3–5 min and the settling/assembling time was set to *ca.* 10 min.

Two-step method

The two-step method is divided into two processes, i.e. the nanoparticle preparation and the hydrogel formation. The process of NH_4F-triggered gelation of NaCA-stabilized gold NP solutions is described here as an example.

Preparation of the Gold Nanoparticle Solution

Aqueous solutions of NaCA (400 mM, 25.0 μL) and $HAuCl_4 \cdot 3H_2O$ (32.5 mM, 30.8 μL) were added successively to 4.88 mL water and stirred for ~2 min. Then freshly prepared $NaBH_4$ aqueous solution (200 mM, 20.0 μL) was rapidly injected, followed by stirring for ca. 2 min. The molar ratio of the metal salt (M), ligand (L), and reductant (R) was fixed at 1 / 10 / 4.

Preparation of the Gold Hydrogel

An aqueous solution of NH_4F (10.0 M, 50 μL) was added to the as-prepared gold NP solution (4.95 mL). After continuously stirring for *ca.* 90 s, the resulting gel pieces were manually assembled together to form a monolithic gel. The fabrication process can be scaled up to 800 mL by using similar procedures.

Dynamic shelling approach (DSA)

Aqueous solutions of NaCA (400 mM, 62.5 μL) and $HAuCl_4 \cdot 3H_2O$ (32.5 mM, 38.5 μL) were added successively to 4.76 mL water under stirring at 600 rpm. Then freshly prepared $NaBH_4$ aqueous solution (200 mM, 50.0 μL) and NH_4F aqueous solution (10.0 M, 50.0 μL) were successively added. After stirring for ca. 15s, an aqueous solution of K_2PtCl_4 (32.5 mM, 38.5 μL) was added. The stirring was continued for ~90 s and the resulting aggregates were manually assembled to yield the final Au-Pt core-shell-structured gel.

Fabrication of Noble Metal Aerogels (NMAs)

The as-prepared hydrogels were washed by a large amount of water for 4–5 times with a total duration of 2–3 days to remove possible residues. Later on, the hydrogels were solvent-exchanged at 303 K with tert-butanol for 2 times. Afterwards, the resulting wet gels were flash-freezed by liquid nitrogen and remained at -196 ºC for ~10 min to enable complete freezing. The frozen samples were put into the chamber of a freeze dryer (TOPTI-12S-80), performing the drying process at ~1 Pa for 12–24 h, where the temperature of the cold trap was set to -80 ºC. The yield of NMAs was calculated based on the mass of the final aerogels with reference to the mass of the corresponding precursor metal salts.

Computational Procedures

Monte–Carlo (MC) simulations

A self-developed random walk Monte-Carlo algorithm was used for simulating the influence of disturbances on the gelation process. The initial positions of particles (the radius is arbitrarily fixed to 3 nm) were generated randomly in a spherical space with a volume of 2.1×10^6 nm^3. All particles were non-interacting. In each Monte-Carlo step, all particles (or aggregates) were either moved translationally or rotated (both with a probability of 50%). If – during translation or rotation – two particles (or aggregates) met, they were considered as one aggregate afterwards. The algorithm was terminated if all particles were aggregated to one single rigid aggregate. Translational movements were performed with a randomly chosen step length (between 0 nm and the maximum step length x, x = 1 nm, 2 nm, and 3 nm). Rotations were performed with a randomly chosen rotation angle (between 0° and 10°).

For the calculation of radius of gyration (R_g), all single particles were neglected (for point-like particles, R_g = 0), and only aggregates (with 2 or more particles) were considered. For the calculation of R_g from a not fully aggregated system (consisting of 2 or more aggregates), the radius of gyration is averaged over all aggregates. The radius of gyration of a single aggregate is calculated as:

$$R_g = \sqrt{\lambda_x^2 + \lambda_y^2 + \lambda_z^2}$$

where λ_x^2, λ_y^2, λ_z^2 are the eigenvalues of the diagonalized radius-of-gyration tensor of the n-particle aggregate:

$$G = \frac{1}{n}\sum_{i=1}^{n}\begin{pmatrix} x_i x_i & x_i y_i & x_i z_i \\ y_i x_i & y_i y_i & y_i z_i \\ z_i x_i & z_i y_i & z_i z_i \end{pmatrix}$$

For each parameter set, 1000 MC runs were performed for statistical analysis.

Characterizations

Microscopy Characterization

Scanning electron microscopy (SEM) analysis was performed on a Zeiss Gemini 500 or a Nova 200 NanoSEM scanning electron microscope. Samples were prepared by directly sticking on conductive tape.

Transmission electron microscopy (TEM) analysis was carried out by using a FEI Tecnai G2 20 or a JEM-2100F microscope operated at 200 kV. Samples were prepared by dispersing in acetone under ultrasonication (15 s to 120 s, depending on their dispersing ability), followed by dropping onto carbon-coated copper grids and drying at ambient temperature.

High-angle annular dark-field scanning transmission electron microscopy (HAADF-STEM) imaging and spectrum imaging based on energy-dispersive X-ray spectroscopy (EDX) were performed at 200 kV with a Talos F200X microscope equipped with an X-FEG electron source and a Super-X EDX detector system (FEI). Prior to STEM analysis, the specimen mounted in a high-visibility low-background holder was placed for 2 s into a Model 1020 Plasma Cleaner (Fischione) to remove possible contamination.

Optical imaging was performed on a Carl Zeiss Microscopy, with the magnification of 63×10.

Diffraction Characterization

X-ray powder diffraction (XRD) was carried out in reflection mode on a Siemens D5000 X-ray diffractometer operated at a voltage of 30 kV and a current of 10 mA with Cu Kα radiation (λ = 1.5406 Å). The data were collected in the range of 20°–90° (2θ) with a step size of $\Delta 2\theta$ = 0.02°. The sample was fixed on the holder by Scotch tape. For the single-metal system, the crystallite size was estimated by the Scherrer equation applying a crystallite-shape factor K = 0.9.

Spectroscopy Characterization

Ultraviolet–visible spectroscopy (UV-vis) absorption spectra were recorded on a Cary 60 UV-Vis Spectrophotometer.

Element Analysis

X-ray photoelectron spectroscopy (XPS) was performed on an Axis Ultra spectrometer (Kratos, UK) with a high-performance Al monochromatic source operated at 15 kV. The XPS spectra were taken after all binding energies were referenced to the C 1s neutral carbon peak at 284.8 eV, and the elemental compositions were determined from the peak area ratios after correction for the sensitivity factor by CasaXPS.

Inductively coupled plasma optical emission spectroscopy (ICP-OES) was performed on a Perkin-Elmer Optima 7000DV optical emission spectrometer.

Gas Adsorption Measurement

Nitrogen adsorption experiments were performed with a Quantachrome NOVA 3000e system at 77 K. The sample was outgassed at 323 K for ~24 h under vacuum before measurement. The filling rod was used to reduce the dead volume, thus improving the measurement accuracy. The specific surface area was calculated by using the multi-point BET equation ($0.1 < p/p_0 < 0.3$). The pore size distribution was derived by using the non-local density functional theory (NLDFT) method (N_2 at 77 K on carbon) based on a slit pore geometry. The total pore volume was calculated at $p/p_0 = 0.99$, similar to the value derived by the BJH (Barret–Joyner–Halender) method. For low-surface-area samples, instead of nitrogen, krypton (Kr) was used as the probe molecule to quantify the specific surface area, due to their lower saturation pressure (≈2.63 Torr for supercooled liquid krypton at 77K) compared to that of nitrogen molecules (≈760 Torr at 77K), thus allowing to acquire a much more accurate result ascribed to a large relative pressure change with a small amount of gas adsorption/desorption.

Electrochemical Measurements

All electrochemical tests were performed with a three-electrode system on an Autolab/PGSTAT 30 (Eco Chemie B. V. Utrecht, the Netherlands) or a CHI potentiostat (CHI 760D). A glassy carbon electrode (GCE, 3 mm in diameter), an Ag/AgCl (saturated KCl aqueous solution) electrode, and a platinum foil were used as working electrode, reference electrode, and counter electrode, respectively.

For modification of the working electrode, ~1.0 mg catalyst was dispersed in 425 μL 2-propanol (IPA) and 75 μL Nafion (1 wt.% in IPA) by sonicating for ca. 30 min to acquire the catalyst ink. Then a specific amount of ink was transferred onto the GCE and evaporated at ambient temperature. The concentrations of Pd and Pt in the ink were determined by ICP-OES, and the total loading of Pd and Pt (m_{Pd+Pt}) was calculated accordingly to ~20 μg cm^{-2}.

For the electro-oxidation of ethanol, the test was performed under N_2 atmosphere in 1.0 M KOH aqueous solution containing 1.0 M ethanol. CV curves were recorded between -0.9 and 0.3 V (*vs.* AgCl/Ag) with a scanning rate of 50 mV s^{-1}. The stability test was conducted at the potential of -0.23 V (*vs.* AgCl/Ag). For the photoelectrocatalysis, a round panel with seven LED lamps (7×OSRAM SSL 80 Streetwhite on round PCB (Color: 5700–7500 K, wavelength 350–800 nm), LED. Tech. The diameter of the panel is 35 mm, white LEDs are evenly distributed on the panel) was closely placed under the electrolytic cell. The LEDs were lightened by a tunable power source. The light power density (0–133.6 mW cm^{-2}) was calibrated by taking advantage of its linear relationship with the input power (**Figure S23a**), which was derived from an optical power meter assuming an even light field distribution and neglecting the interactions between light and the electrolyte solution.

Figures

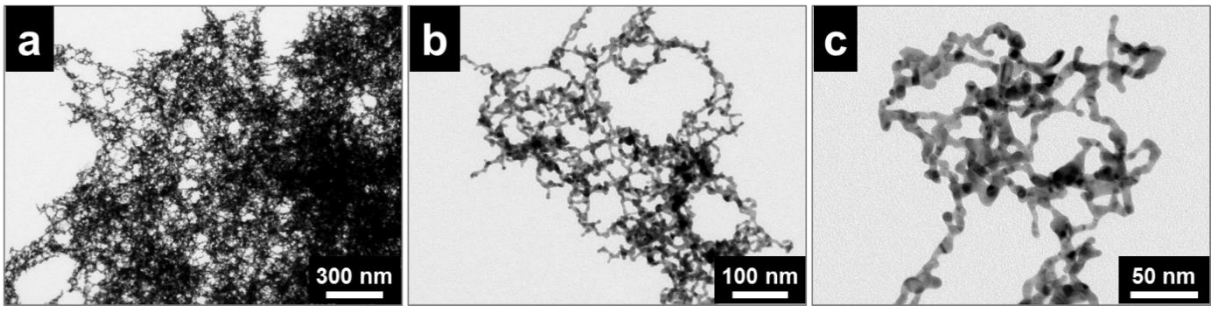

Figure S1. TEM images of gold aggregates after addition of NH_4F to NaCA-stabilized gold NP solutions (c_M = 0.2 mM) and stirring for 45 s.

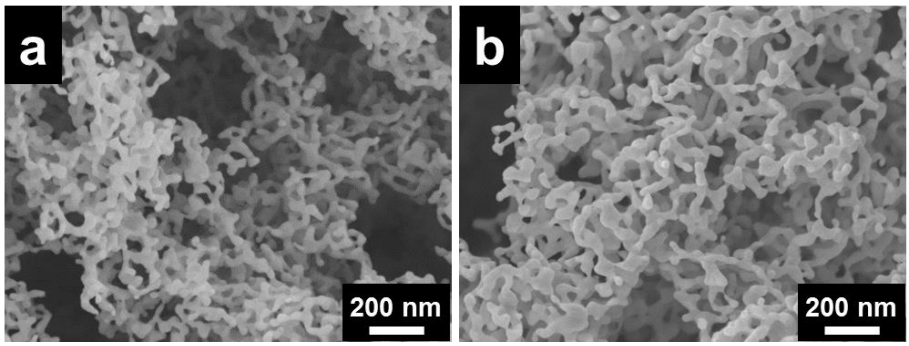

Figure S2. SEM images of gold aerogels prepared by NH_4F-induced gelation under (a) static and (b) stirring environment.

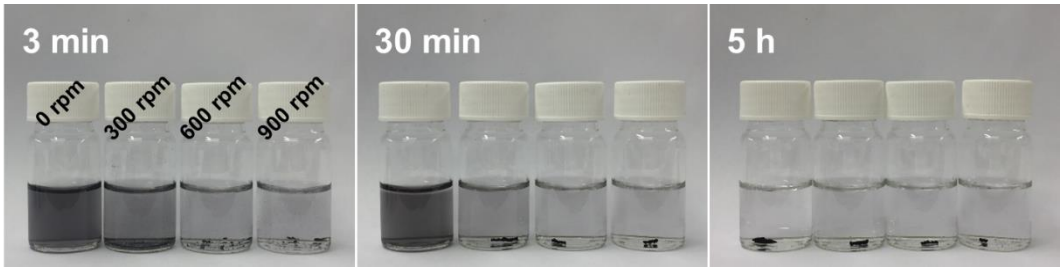

Figure S3. Time-lapse photographs of the gelation process of gold NP solutions (triggered by NH_4F) under stirring at different speed (0, 300, 600, and 900 rpm) for 2 min.

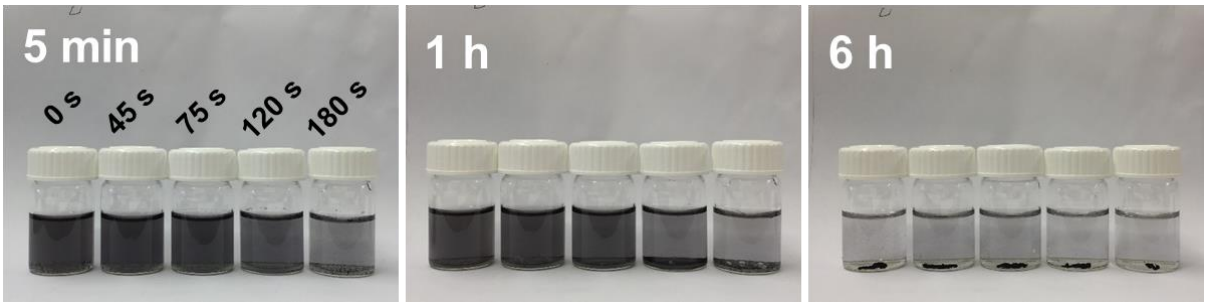

Figure S4. Time-lapse photographs of the gelation of gold NP solutions (triggered by $NaBH_4$) under stirring at 600 rpm for 0, 45, 75, 120, and 180 s.

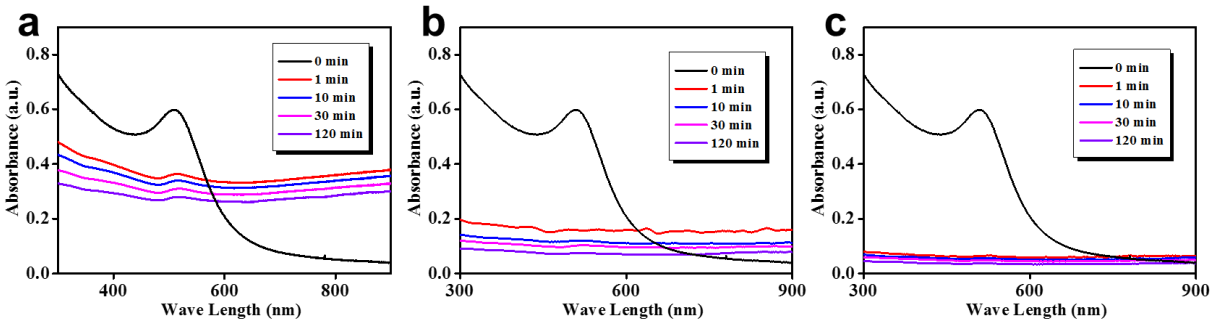

Figure S5. Time-lapse UV-vis spectra of NaCA-stabilized gold NP solutions (c_M = 0.2 mM) after initiation by NH_4F and subsequent stirring for (a) 0 s, (b) 45 s, and (c) 120 s.

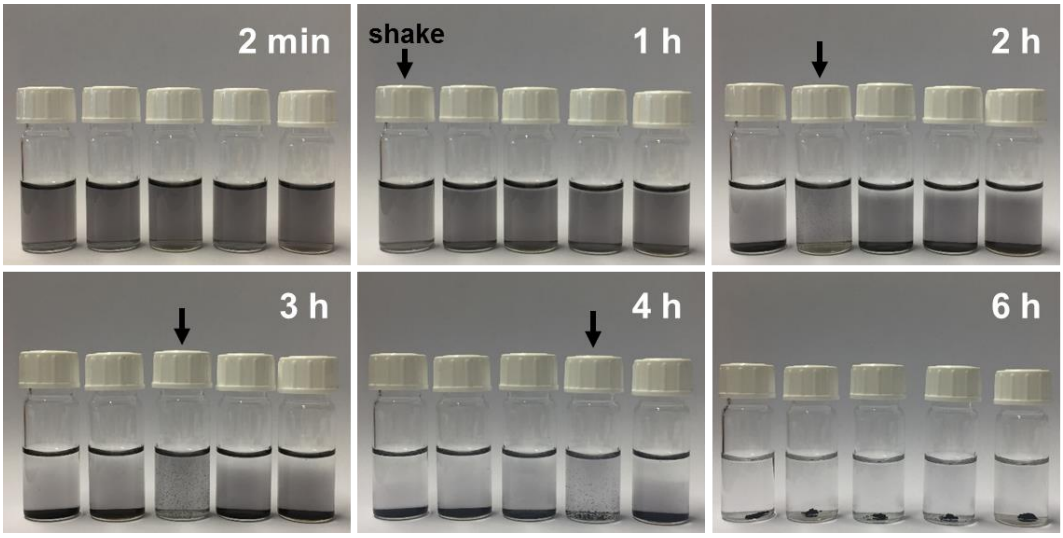

Figure S6. The gelation process of gold NP solutions (triggered by NH_4F) with disturbance introduced at different stages. From left to right vials, the gelation systems were disturbed at 1 h, 2 h, 3 h, 4 h, and without disturbance.

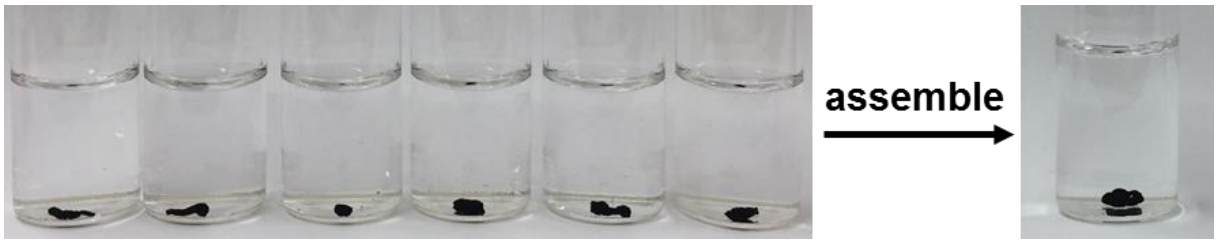

Figure S7. Several as-formed gold hydrogels assemble together into one self-supported hydrogel.

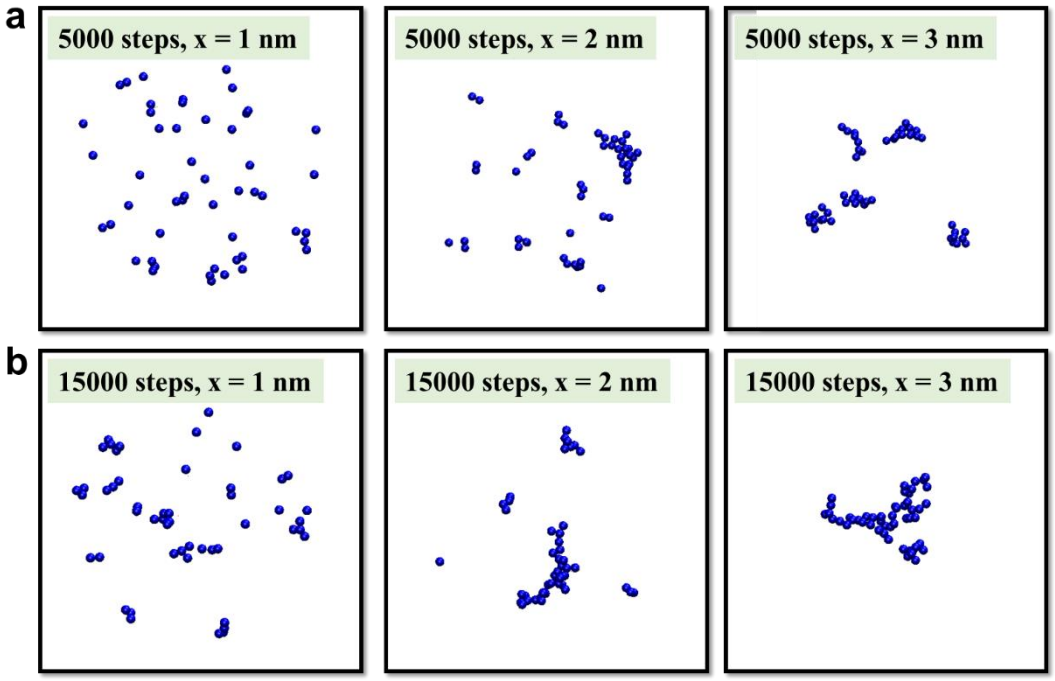

Figure S8. Figures from MC simulations. The aggregation status of particles after (a) 5000 steps and (b)15000 steps with indicated maximum step length x (x=1, 2, 3 nm).

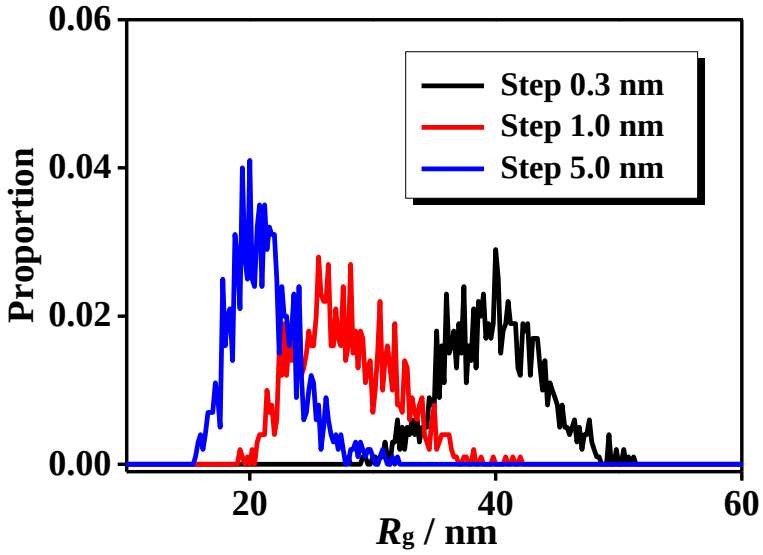

Figure S9. The distribution of the radius of gyration (R_g) of the final single aggregate resulting from MC simulations with different maximum step lengths.

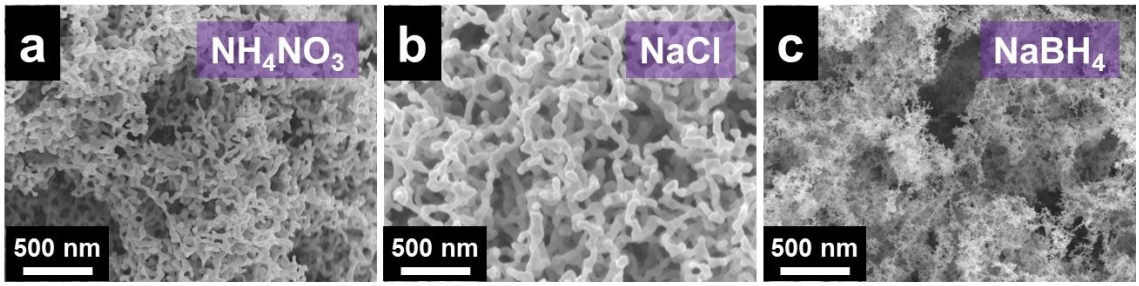

Figure S10. SEM images of stirring-promoted gold gels initiated by different means. Gelation was induced by (a) NH_4NO_3 and (b) NaCl for NaCA-stabilized gold NP solutions, and (c) $NaBH_4$ for PVP-stabilized gold NP solutions.

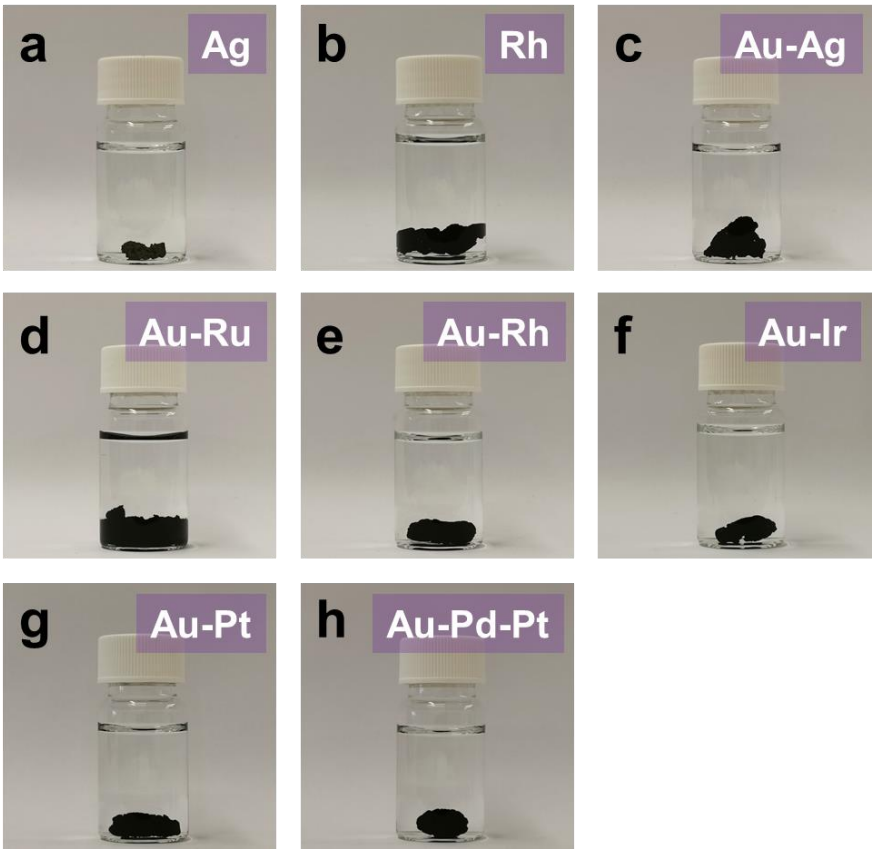

Figure S11. Photographs of noble metal hydrogels with diverse compositions made by the stirring-promoted gelation process initiated by NH_4F.

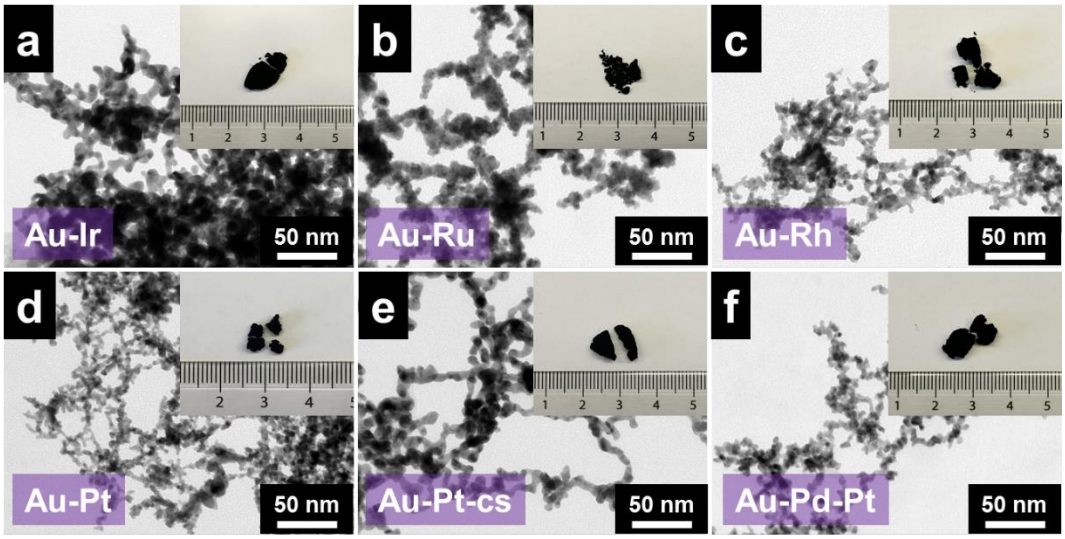

Figure S12. TEM images and photographs (inset) of diverse multimetallic aerogels. Au-Pt-cs indicates the core-shell-structured Au-Pt aerogel.

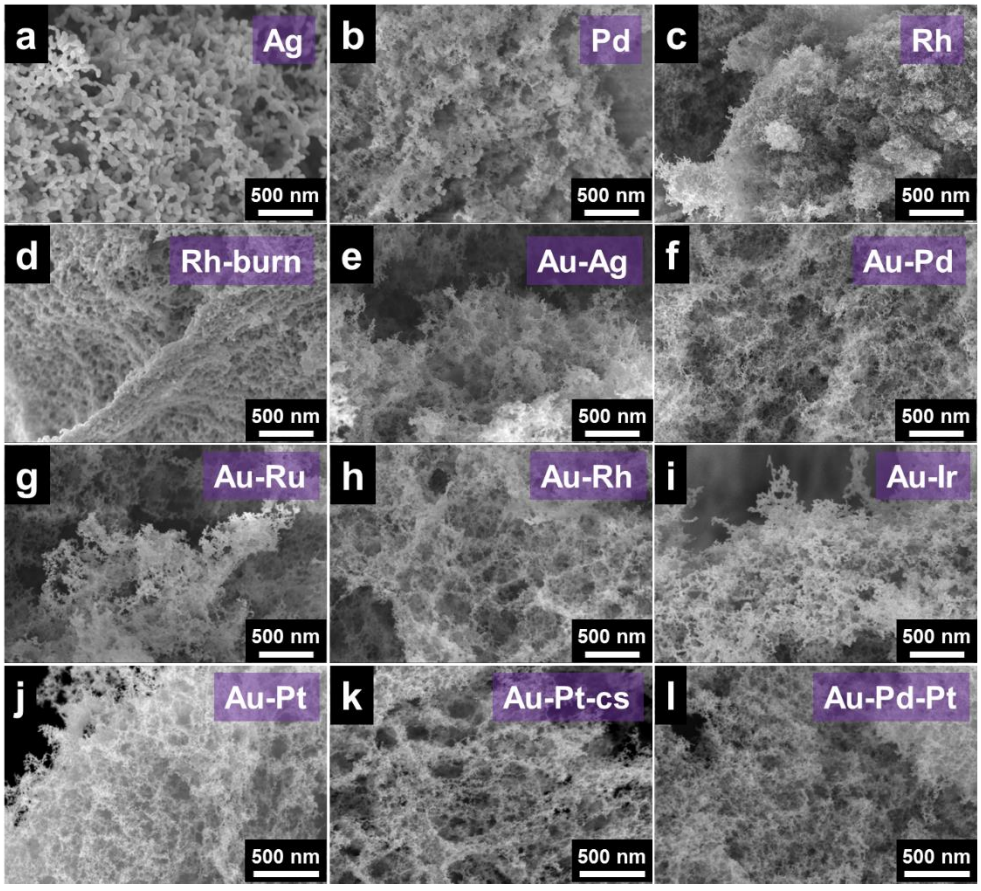

Figure S13. SEM images of noble metal aerogels with diverse compositions. Rh-burn indicates the Rh aerogel after its spontaneous combustion in air.

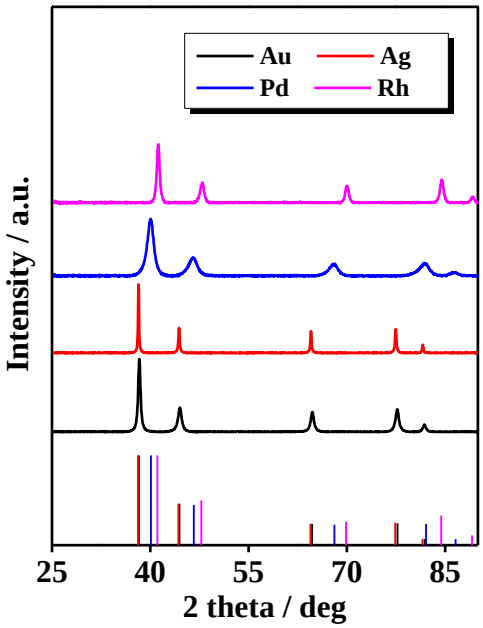

Figure S14. XRD patterns of diverse monometallic aerogels.

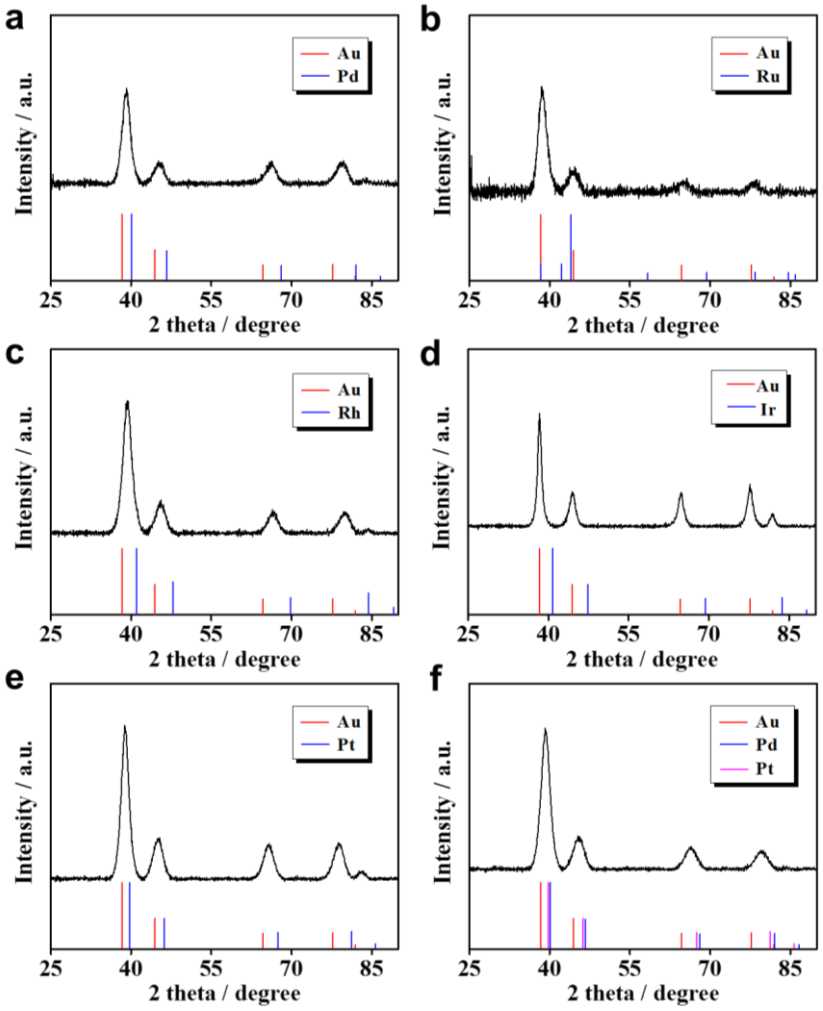

Figure S15. XRD patterns of diverse multimetallic aerogels, (a) Au-Pd, (b) Au-Ru, (c) Au-Rh, (d) Au-Ir, (e) Au-Pt, (f) Au-Pd-Pt.

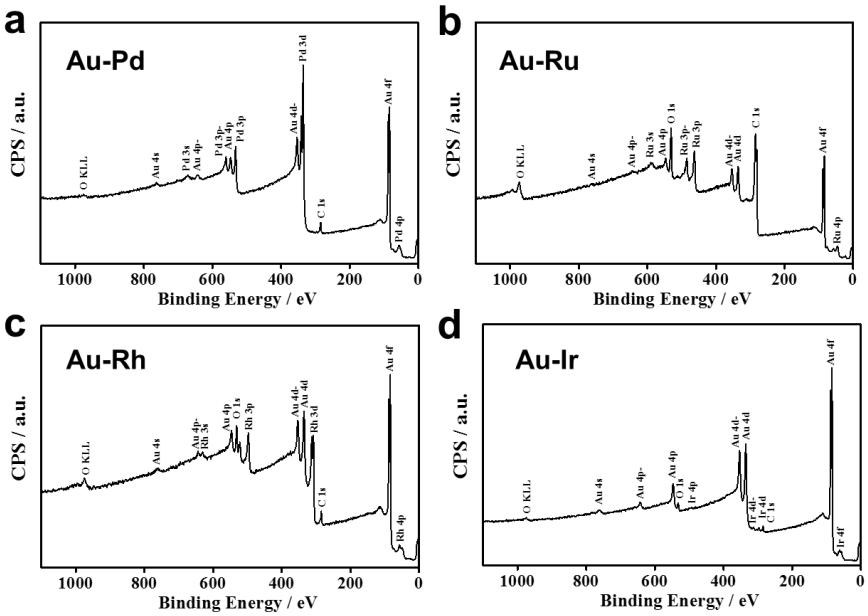

Figure S16. XPS spectra of several bimetallic aerogels, (a) Au-Pd, (b) Au-Ru, (c) Au-Rh, and (d) Au-Ir.

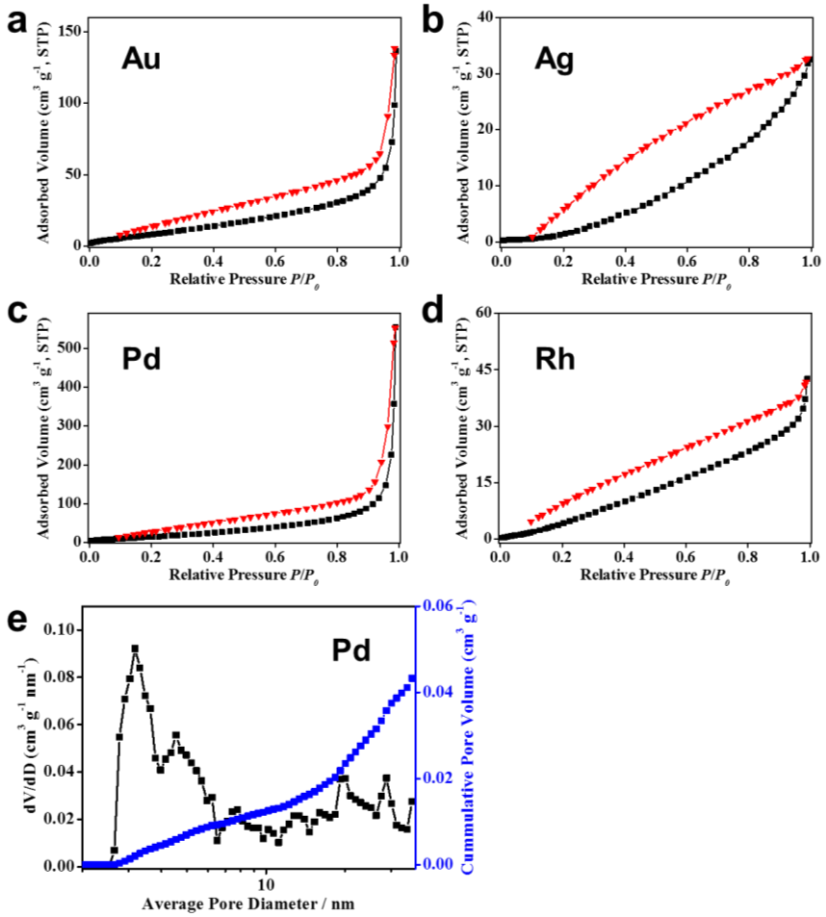

Figure S17. Nitrogen adsorption test of diverse monometallic aerogels. Adsorption/desorption isotherms of (a) Au, (b) Ag, (c) Pd, and (d) Rh aerogels. (e) Pore size distribution of Pd aerogel. The Au gel was fabricated from PVP-stabilized gold NP solution as triggered by $NaBH_4$.

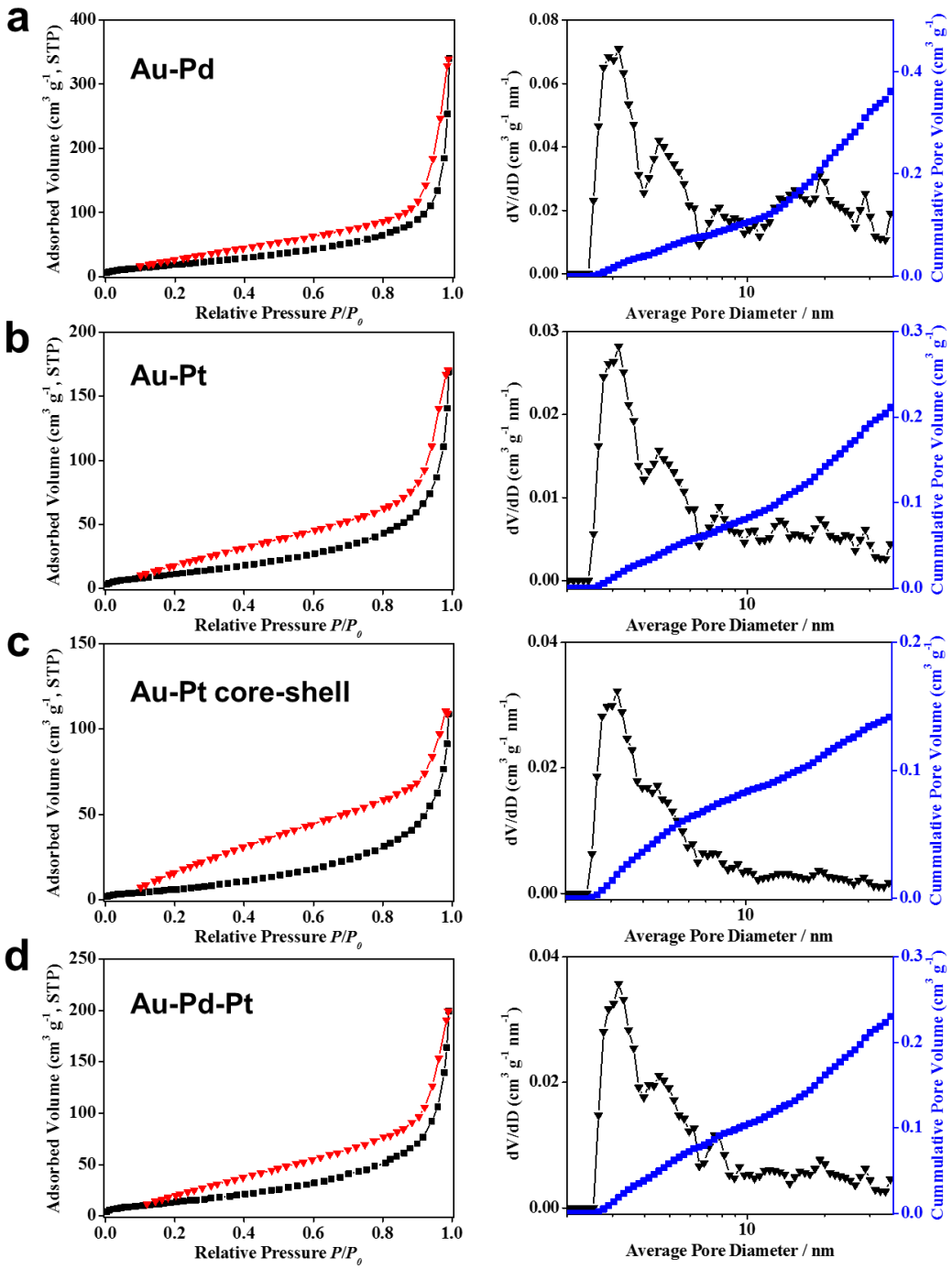

Figure S18. Adsorption/desorption isotherms and pore size distributions of diverse multimetallic aerogels, (a) Au-Pd, (b) Au-Pt, (c) Au-Pt core-shell, and (d) Au-Pd-Pt.

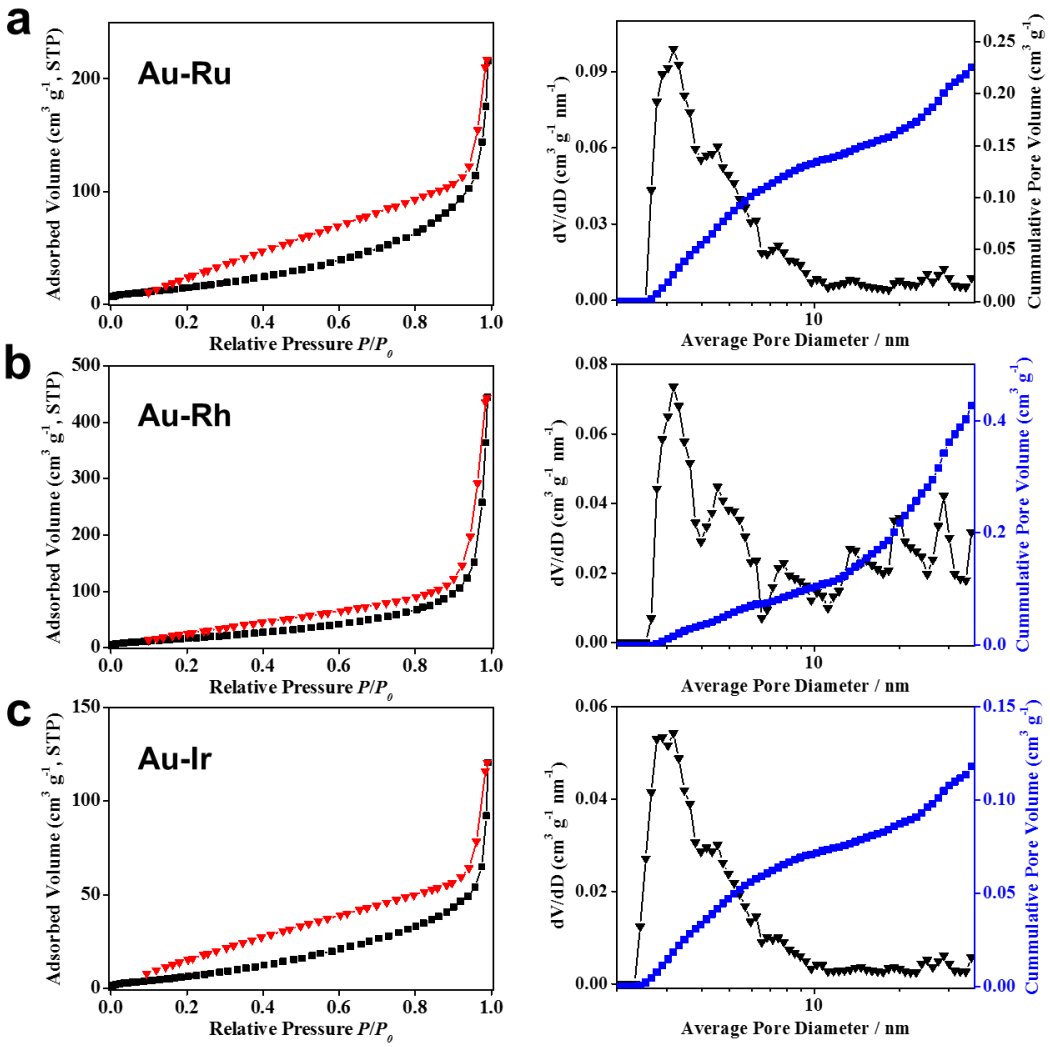

Figure S19. Adsorption/desorption isotherms and pore size distribution of several bimetallic aerogels, (a) Au-Ru, (b) Au-Rh, and (c) Au-Ir.

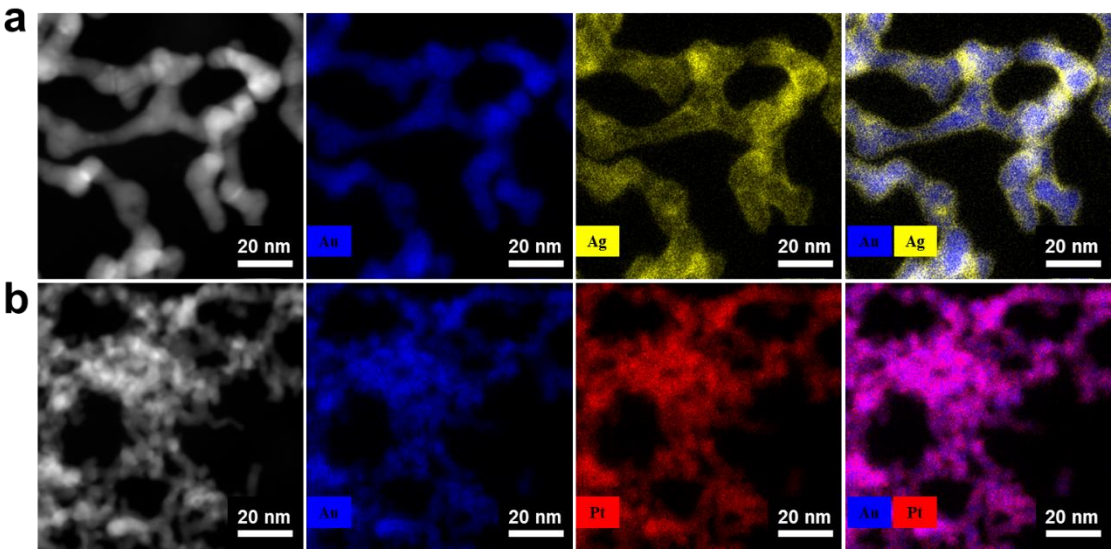

Figure S20. HAADF-STEM imaging and corresponding EDX mapping of multimetallic aerogels, (a) Au-Ag and (b) Au-Pt.

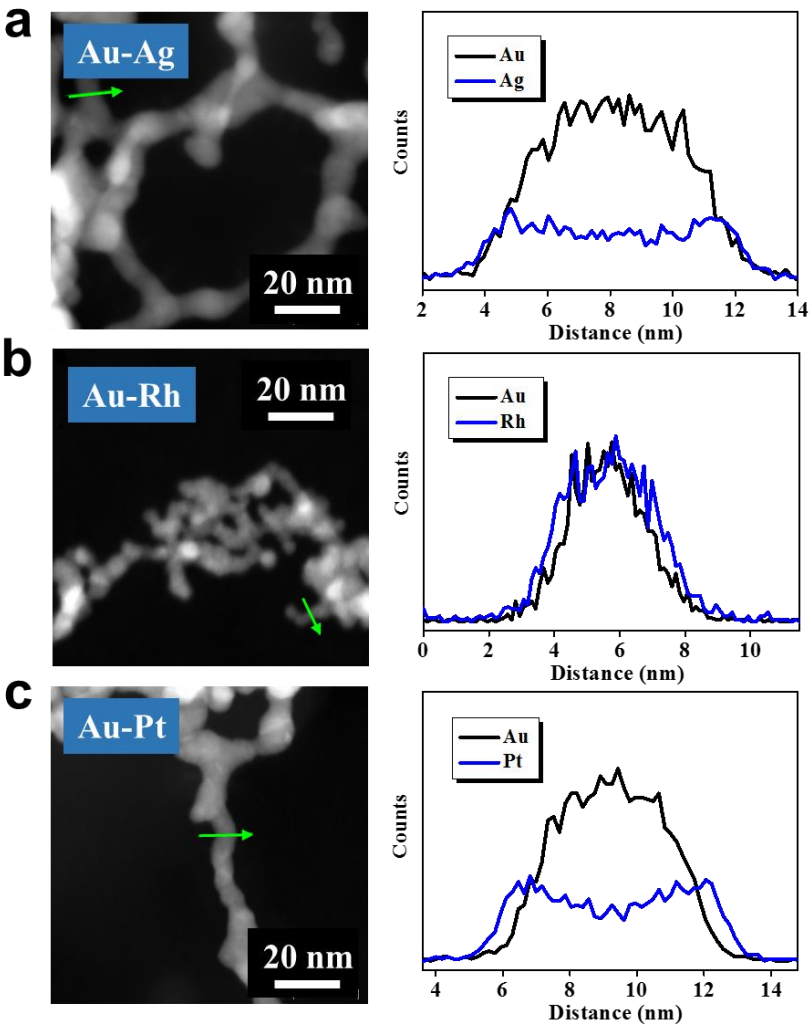

Figure S21. HAADF-STEM imaging and EDX analysis (line scan) of core-shell-structured multimetallic aerogels. The (a) Au-Ag gel and (b) Au-Rh gel were fabricated by directly triggering Au-Ag NP solution with NH_4F. (c) The Au-Pt gel was fabricated by combining the stirring-promoted gelation strategy a dynamic shelling approach.

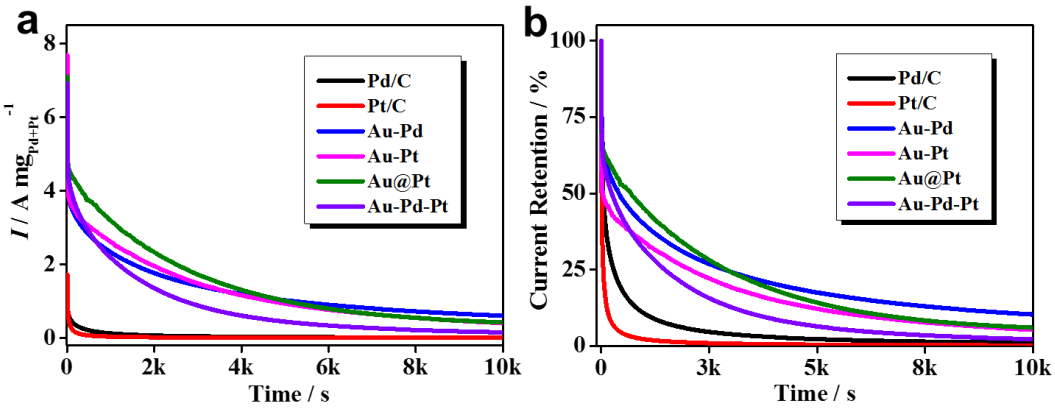

Figure S22. Chronoamperometry tests of various commercial and aerogel electrocatalysts.

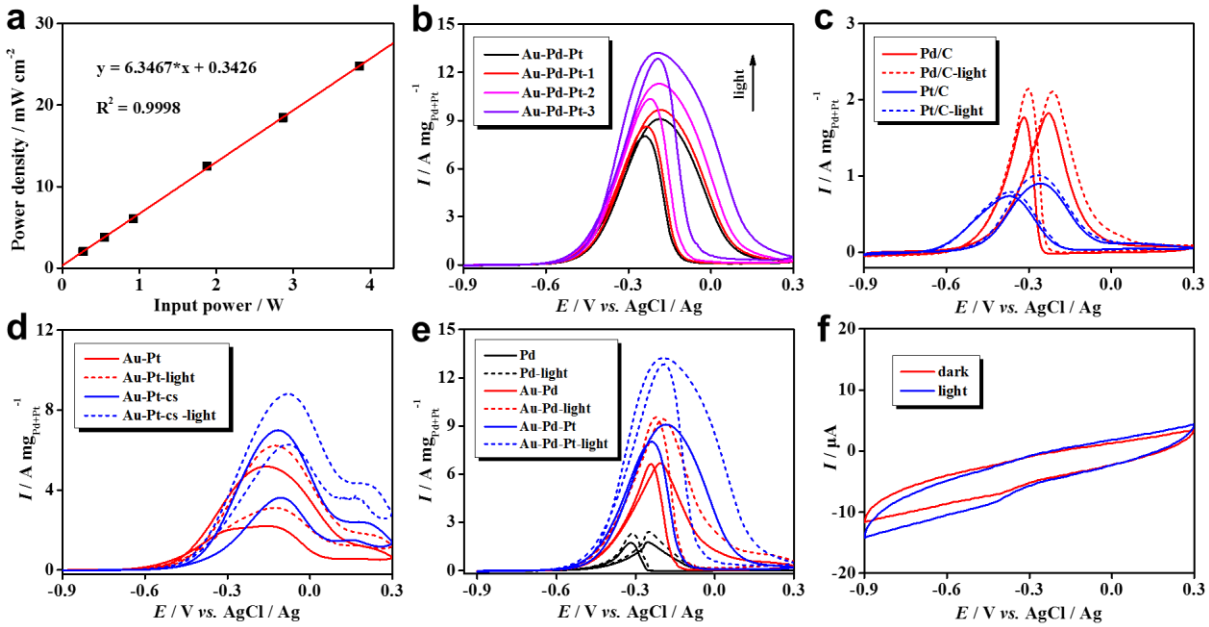

Figure S23. Characterization of the photoelectrocatalytic EOR properties. (a) Linear fitting of the areal light power density of the employed LEDs against the input electrical power. (b) EOR performance of the Au-Pd-Pt aerogel under different light power densities (Au-Pd-Pt denote the dark condition; Au-Pd-Pt-1, 2, 3 denote the light power densities of 12.3, 64.1, and 133.6 mW cm^{-2}, respectively). (c-e) EOR performance of various commercial and aerogel catalysts under dark and light condition (light density of 133.6 mW cm^{-2}). (f) EOR performance on a blank glassy carbon electrode under dark and light condition. All tests were performed in N_2-saturated 1.0 M KOH + 1.0 M ethanol solution at a scan rate of 50 mV s^{-1}.

Tables

Table S1. Comparison of the fabrication conditions of noble metal gels reported in literature.

Metals	Concentrations	Methods	Gelation Time	Ref
Au, Ag, Pd, Rh, Au-Ag, Au-Pd, Au-Pt, Au-Rh, Au-Ru, Au-Ir, Au-Pt core-shell, Au-Pd-Pt	0.02–5.0 mM	Salts or $NaBH_4$ under a disturbing environment	1–10 min	**This work**
Au	0.22 mM	Dopamine	6–72 h	1
Au	0.2 mM	Glucose	~12 h	2
Ag	37.5 mM	$(C(NO_2)_4$	4–12 h	3
Pd	0.8 mM	Glyoxylic acid, sodium carbonate & ~338 K	~1 h	4
Pd	~6.6 mM	In acetic acid, CO & 313 K	5 h	5
Pd	~17 mM	Ca^{2+}	5 min to 2 months	6
Pd	0.2 mM	$NaBH_4$, β-CD	3–10 d	7
Pt	~15 mM	N_2H_4 (in hexane)	1–5 h	8
Au, Pd, Pt	5–100 mM	$NaBH_4$, NaH_2PO_2, or Dimethylamine borane	A few minutes	9
Au, Ag, Pt, Au-Ag, Ag-Pt	10 mM	Ultracentrifugation & H_2O_2	1–4 weeks	10
Au, Ag, Pd, Pt, Au-Ag, Au-Pd, Au-Pt, Pd-Pt, Au-Pd-Pt	0.02–2 mM	Salts	4–48 h	11
Au, Ag, Pd, Pt, Ag–Pd, Ag–Au, Pt–Pd, Ag-Au-Pd	12–24 mM	Hydrazine, 333 K	Several hours	12
AuCu, PdCu, PtCu	0.3 mM	$NaBH_4$, 333 K	6 h	13
Au-Pt	0.6 mM	$NaBH_4$, 333 K	2–4 h	14
Au-Cu	≥ 8 mM	$NaBH_4$	Several minutes	15
Pd-Pt	0.2 mM	$NaBH_4$	3–17 d	16
Pd-Ni	60 mM	Ultracentrifugation, $NaBH_4$, 348 K	< 6 h	17
Pd_xPt_y-Ni	60 mM	Ultracentrifugation, $NaBH_4$, 348 K	< 6 h	18
Pd-Cu	0.3 mM	$NaBH_4$, 333 K	6 h	19
Ir_xCu	1.3 mM	$NaBH_4$, 343 K	2–3 h	20
Au-Ag-Pd	~3 mM	Ultracentrifugation, $(C(NO_2)_4$	16–24 h	21

Table S2. Summary of nitrogen adsorption data and ligament sizes of as-prepared aerogels. The specific surface area S_{BET} (m^2 g^{-1}) was calculated in the partial pressure (p/p_0) range of 0.1–0.3. The total pore volume V_{tot} is derived at p/p_0 =0.99. The average ligament size d is derived from a statistic analysis of TEM measurements.

Entry	Metals	Ligands	Initiators	S_{BET} (m^2 g^{-1})	V_{tot} (cm^3 g^{-1})	d (nm)
1	Au[a]	NaCA	NH_4F	/	/	19.8 ± 3.7
2	Au[a]	PVP	$NaBH_4$	42.6	0.211	10.4 ± 3.1
3	Ag	NaCA	NH_4F	/	/	18.1 ± 3.0
4	Pd	NaCA	NH_4F	76.6	0.857	5.8 ± 1.2
5	Rh[b]	NaCA	NH_4F	38.0	0.245	4.1 ± 0.5
6	Au-Ag[c]	NaCA	NH_4F	/	/	7.1 ± 1.0
6	Au-Pd	NaCA	NH_4F	83.6	0.526	3.9 ± 0.6
7	Au-Pt	NaCA	$NaBH_4$	51.5	0.261	3.7 ± 0.7
8	Au-Pt (core-shell)	NaCA	NH_4F	32.0	0.168	5.3 ± 0.7
9	Au-Rh	NaCA	NH_4F	78.3	0.687	4.6 ± 1.2
10	Au-Ir	NaCA	$NaBH_4$	40.9	0.186	7.2 ± 1.8
11	Au-Pd-Pt	NaCA	NH_4F	60.2	0.309	4.3 ± 0.6

[a] The total concentration of the metal salt precursor was 0.2 mM. For other entries, the concentration was 0.5 mM.

[b] The gel can undergo spontaneous combustion when exposed to air. All parameters were obtained from unburned aerogels.

[c] For the multimetallic systems, the molar ratio of the different metals in the original metal solution is set equally.

References

1. Wen, D., Liu, W., Haubold, D., Zhu, C., Oschatz, M., Holzschuh, M., Wolf, A., Simon, F., Kaskel, S., Eychmüller, A., (2016). Gold Aerogels: Three-Dimensional Assembly of Nanoparticles and Their Use as Electrocatalytic Interfaces. ACS Nano *10*, 2559-2567.

2. Qin, G. W., Liu, J., Balaji, T., Xu, X., Matsunaga, H., Hakuta, Y., Zuo, L., Raveendran, P., (2008). A Facile and Template-Free Method to Prepare Mesoporous Gold Sponge and Its Pore Size Control. J. Phys. Chem. C *112*, 10352-10358.

3. Gao, X., Esteves, R. J., Luong, T. T. H., Jaini, R., Arachchige, I. U., (2014). Oxidation-Induced Self-Assembly of Ag Nanoshells into Transparent and Opaque Ag Hydrogels and Aerogels. J. Am. Chem. Soc. *136*, 7993-8002.

4. Douk, A. S., Saravani, H., Noroozifar, M., (2018). Three-Dimensional Assembly of Building Blocks for the Fabrication of Pd Aerogel as a High Performance Electrocatalyst toward Ethanol Oxidation. Electrochim. Acta *275*, 182-191.

5. Yazdan-Abad, M. Z., Noroozifar, M., Alam, A. R. M., Saravani, H., (2017). Palladium Aerogel as a High-Performance Electrocatalyst for Ethanol Electro-Oxidation in Alkaline Media. J. Mater. Chem. A *5*, 10244-10249.

6. Wen, D., Herrmann, A.-K., Borchardt, L., Simon, F., Liu, W., Kaskel, S., Eychmüller, A., (2014). Controlling the Growth of Palladium Aerogels with High-Performance toward Bioelectrocatalytic Oxidation of Glucose. J. Am. Chem. Soc. *136*, 2727-2730.

7. Liu, W., Herrmann, A. K., Geiger, D., Borchardt, L., Simon, F., Kaskel, S., Gaponik, N., Eychmüller, A., (2012). High-Performance Electrocatalysis on Palladium Aerogels. Angew. Chem. Int. Ed. *51*, 5743-5747.

8. Naskar, S., Freytag, A., Deutsch, J., Wendt, N., Behrens, P., Köckritz, A., Bigall, N. C., (2017). Porous Aerogels from Shape-Controlled Metal Nanoparticles Directly from Nonpolar Colloidal Solution. Chem. Mater. *29*, 9208-9217.

9. Burpo, F. J., Nagelli, E. A., Morris, L. A., McClure, J. P., Ryu, M. Y., Palmer, J. L., (2017). Direct Solution-Based Reduction Synthesis of Au, Pd, and Pt Aerogels. J. Mater. Res. *32*, 4153-4165.

10. Bigall, N. C., Herrmann, A. K., Vogel, M., Rose, M., Simon, P., Carrillo-Cabrera, W., Dorfs, D., Kaskel, S., Gaponik, N., Eychmüller, A., (2009). Hydrogels and Aerogels from Noble Metal Nanoparticles. Angew. Chem. Int. Ed. *48*, 9731-9734.

11. Du, R., Hu, Y., Hübner, R., Joswig, J.-O., Fan, X., Eychmüller, A., (2019). Specific Ion Effects Directed Noble Metal Aerogels: Versatile Manipulation for Electrocatalysis and Beyond. Sci. Adv. *5*, eaaw4590.

12. Tang, S., Vongehr, S., Wang, Y., Cui, J., Wang, X., Meng, X., (2014). Versatile Synthesis of High Surface Area Multi-Metallic Nanosponges Allowing Control over Nanostructure and Alloying for Catalysis and Sers Detection. J. Mater. Chem. A *2*, 3648-3660.

13. Zhu, C., Shi, Q., Fu, S., Song, J., Xia, H., Du, D., Lin, Y., (2016). Efficient Synthesis of MCu (M= Pd, Pt, and Au) Aerogels with Accelerated Gelation Kinetics and Their High Electrocatalytic Activity. Adv. Mater. *28*, 8779-8783.

14. Shi, Q., Zhu, C., Du, D., Bi, C., Xia, H., Feng, S., Engelhard, M. H., Lin, Y., (2017). Kinetically Controlled Synthesis of AuPt Bi-Metallic Aerogels and Their Enhanced Electrocatalytic Performances.

J. Mater. Chem. A *5*, 19626-19631.

15. Wang, J., Chen, F., Jin, Y., Johnston, R. L., (2018). Gold–Copper Aerogels with Intriguing Surface Electronic Modulation as Highly Active and Stable Electrocatalysts for Oxygen Reduction and Borohydride Oxidation. ChemSusChem *11*, 1354-1364.
16. Liu, W., Rodriguez, P., Borchardt, L., Foelske, A., Yuan, J., Herrmann, A. K., Geiger, D., Zheng, Z., Kaskel, S., Gaponik, N., (2013). Bimetallic Aerogels: High-Performance Electrocatalysts for the Oxygen Reduction Reaction. Angew. Chem. Int. Ed. *52*, 9849-9852.
17. Cai, B., Wen, D., Liu, W., Herrmann, A. K., Benad, A., Eychmüller, A., (2015). Function-Led Design of Aerogels: Self-Assembly of Alloyed PdNi Hollow Nanospheres for Efficient Electrocatalysis. Angew. Chem. Int. Ed. *54*, 13101-13105.
18. Cai, B., Dianat, A., Hübner, R., Liu, W., Wen, D., Benad, A., Sonntag, L., Gemming, T., Cuniberti, G., Eychmüller, A., (2017). Multimetallic Hierarchical Aerogels: Shape Engineering of the Building Blocks for Efficient Electrocatalysis. Adv. Mater. *29*, 1605254.
19. Lu, L., Sun, X., Ma, J., Yang, D., Wu, H., Zhang, B., Zhang, J., Han, B., (2018). Highly Efficient Electroreduction of Co2 to Methanol on Palladium–Copper Bimetallic Aerogels. Angew. Chem. Int. Ed. *57*, 14149-14153.
20. Shi, Q., Zhu, C., Zhong, H., Su, D., Li, N., Engelhard, M. H., Xia, H., Zhang, Q., Feng, S., Beckman, S. P., et al., (2018). Nanovoid Incorporated Ir_xCu Metallic Aerogels for Oxygen Evolution Reaction Catalysis. ACS Energy Lett. *3*, 2038-2044.
21. Nahar, L., Farghaly, A. A., Esteves, R. J. A., Arachchige, I. U., (2017). Shape Controlled Synthesis of Au/Ag/Pd Nanoalloys and Their Oxidation-Induced Self-Assembly into Electrocatalytically Active Aerogel Monoliths. Chem. Mater. *29*, 7704-7715.